

Assessing Feasible Gait Dynamics of a Highly Coupled Quadruped Robot with Six Actuated Degrees of Freedom

Scientific work for obtaining the academic degree

Master of Science (M.Sc.)

at the School of Engineering and Design of the Technical University of Munich

Supervised by Prof. Dr. Alin Albu-Schäffer
Florian Christoph Loeffl
TUM School of Computation, Information and Technology (CIT)

Submitted by Pirmin Gaißer
Schanzenbachstraße 13
81371 München

Submitted on December 2, 2024 in Garching

Institute of Robotics and Mechatronics
German Aerospace Center (DLR)



Task Description

Assessing Feasible Gait Dynamics of a Highly Coupled Quadruped Robot with Six Actuated Degrees of Freedom

Author: Pirmin Gaißer
Registration: October 1 2024

Supervisor: Florian Christoph Loeffl
Submission: December 2 2024

Introduction:

Legged robots are often hindered by challenges related to energy efficiency and system reliability, mainly due to the use of multiple actuators. Conventional quadruped designs typically feature 12 actuated degrees of freedom (DoF), allowing for a high degree of flexibility in foot placement and body positioning. In contrast, this project investigates a quadruped robot with only six actuated DoF, where each motor is linked to multiple legs.

Objective and Expected Outcome:

The primary objective of this project is to assess the feasibility of gait dynamics for a 6 DoF quadruped robot, building upon an optimized geometry developed during my semester thesis. The proposed design will require slight modifications to facilitate its construction and testing in real-world conditions. The project will proceed through several key phases:

1. Design and Simulation: The robot will first be modeled in Creo (CAD software), and its kinematic and geometric data will be exported into Mujoco (simulation software). The walking patterns, coded in Python, will be tested within this environment. Key concepts such as static stability, gait cycles, and inverse kinematics will be explored to identify viable motor movements that can produce stable gaits.
2. Construction: Once stable gaits are achieved in simulation, the robot will be constructed using servo motors, a servo controller, a microcontroller, and 3D-printed components alongside standard parts like bearings and bolts. This phase will test whether quasi-static walking patterns can be realized in the real world, and explore any limitations that arise.

Garching, December 02, 2024

Prof. Dr.-Ing
Alin Albu-Schäffer

Dipl.-Ing.
Florian C. Loeffl

(B.Sc.)
Pirmin Gaißer

Abstract

This thesis explores the feasibility of stable gait dynamics in a quadruped robot with six actuated degrees of freedom (DoF). Unlike conventional quadrupeds with twelve actuated DoF, this novel design employs a highly coupled structure, with each actuator influencing multiple legs. The reduction in DoF presents significant challenges in terms of locomotion control, workspace and stability during motion. The primary objective is to develop and validate quasi-static crawling gaits that maintain stability despite the robot's constrained body workspace.

The work begins by analyzing the coupled kinematic design, which was optimized in previous research (GAISSER 2024), to understand its constraints and motion capabilities. Using a parameterized approach, feasible gaits are identified through a combination of sampling in a configuration space and simulation-based evaluations. The sampling framework assesses stability at critical transition points in the gait cycle, using metrics such as stability margins, joint limits, and workspace constraints. Additionally, inverse kinematics are solved through simulation to generate joint trajectories, addressing the unique challenges posed by the coupled kinematic chains and singularities in the design.

A prototype robot was developed to physically test the feasibility of the proposed gaits. The hardware was carefully designed accounting for practical considerations such as motor torque, link stiffness, and collision avoidance. Simulation results demonstrate the feasibility of straight and spinning crawling gaits, and these were further validated experimentally with the physical robot on flat surfaces.

This research demonstrates the viability of stable crawling in quadrupeds with six actuated Degrees of Freedom (DoF), offering insights into locomotion strategies for underactuated robotic systems with highly coupled kinematics. The findings suggest potential pathways for extending this work to dynamic gaits, adaptive control, and more complex terrains, paving the way for cost-effective and energy-efficient quadruped robots in diverse applications.

Contents

List of Abbreviations	vii
1 Introduction	1
1.1 Background	1
1.1.1 Gait	1
1.1.2 Quadrupeds	3
1.2 Goals	5
1.3 Design of the Robot	5
2 Method Selection	7
2.1 Identify Motion Space	7
2.2 Assessing feasible gaits in parameterized foot space	8
2.3 Sampling in configuration space	10
2.4 Path generation	11
2.5 Inverse kinematics	11
2.6 Test motor trajectories	12
2.7 Mechanical Design	12
3 Gait Generation	13
3.1 Constraints and Requirements for Feasibility in Crawling Gaits	13
3.2 Boundaries of the Search Space	14
3.3 Gait Assessment using the Parameter Space Approach	17
3.3.1 Configuration Evaluation	18
3.3.2 Sample Evaluation	20
3.3.3 Path Evaluation	22
3.4 Inverse Kinematics	23
3.4.1 Singularities	23
3.4.2 Assembly Modes	24
3.4.3 Calculation using the QP-Optimization Method	25
3.5 Results	26
3.5.1 Results from Sampling at the Transition Points	26
3.5.2 Gait Results	29
4 Hardware	33
4.1 Design Process	33
4.2 Mechatronic and Mechanic Design	36
5 Validation	39
5.1 Validation in Simulation	39
5.1.1 Simulation of Crawling Gait	40
5.1.2 Simulation of Spinning Gait	42

5.2	Validation on Hardware	44
5.2.1	Validation of Crawling Gait	44
5.2.2	Validation of Spinning Gait	44
6	Discussion, Conclusion and Outlook	47
6.1	Discussion	47
6.2	Conclusion	49
6.3	Outlook	50
A	Image Sequences for Crawling and Spinning Gaits	53
B	Technical Drawing	57
	Bibliography	67

List of Abbreviations

CLIK	Closed-Loop Inverse Kinematics
CoM	Center of Mass
CPG	Central Pattern Generator
DoF	Degrees of Freedom
FK	Forward Kinematics
IK	Inverse Kinematics
PWM	Pulse-Width-Modulation
QP	Quadratic Programming
RBM	Rigid Body Motion
SP	Support Polygon

Chapter 1

Introduction

Legged robots offer significant advantages in terms of mobility and dynamic capabilities compared to wheeled robots. Yet, they are often hindered by challenges related to energy efficiency and system reliability. One direction of research to address these problems is to reduce the number of DoF and used actuators. Conventional quadruped designs typically feature twelve actuated DoF, allowing for a high degree of flexibility in foot placement and body positioning. In contrast, this project investigates a quadruped robot with only six actuated DoF, where each motor is linked to multiple legs. This design results in a reduced body workspace and presents unique challenges in terms of locomotion. The aim of this project is to assess feasible gait dynamics for this reduced-DoF robot, focusing primarily on quasi-static crawling, with some additional dynamic considerations. Ultimately, the robot will be designed, built, and tested, incorporating an optimized geometry from previous research (GAISSER 2024).

1.1 Background

In this chapter, foundational work in robotic quadrupedal locomotion is reviewed, with a particular focus on gait strategies and the design principles underlying quadruped prototypes with reduced DoF. The section details the gait mechanisms and categorization for achieving stable crawling in quadrupeds and introduces various designs that employ fewer actuators. It explores how these reduced-DoF configurations affect locomotion capabilities, stability, and workspace. Additionally, it examines how different quadruped designs balance or trade-offs between movement flexibility, underactuation, and redundancy, especially in crawling gaits. This background provides essential context for the possibilities and constraints present in the proposed robot.

1.1.1 Gait

During crawling, each leg is lifted individually while the other stays on the ground. In each gait cycle, four transition points occur, where all four legs are on the floor simultaneously, as shown in the gait diagram in Figure 1.1.

In this context, quasi-static stability means the Center of Mass (CoM) is always in the support polygon formed by the stance feet. It assumes the locomotion is infinitely slow so that all dynamic effects vanish. Dynamic stability includes the dynamics in the stability considerations.

This work focuses on quasi-static crawling and hence uses slow movements to approximate the stability model. Exceptions are bi-stable configurations. They occur every time one leg is lifted. Switching between stable orientations is exploited in this work.

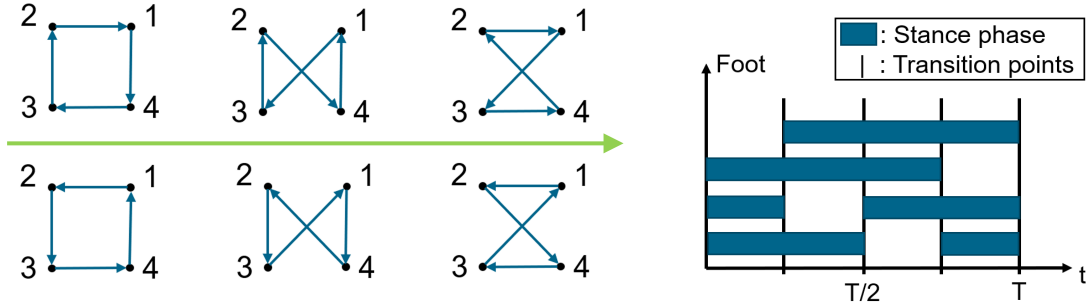


Figure 1.1: All six gait sequences as defined by MCGHEE 1968 relative to the crawling direction marked with the green arrow (left) and the visualization of the gait diagram for crawling sequence [1,3,4,2] (right). Each leg is lifted individually, and four transition points occur.

There are several categorizations for crawling gaits used in literature (GONZALEZ DE SANTOS et al. 2006, MAHAPATRA et al. 2020). First, gaits can be differentiated into periodic and free. While in periodic gaits, the motion repeats at some point, in free gaits, each foot can be placed individually. After one gait cycle, each leg moves once. With a period of one, the initial configuration is reached after one cycle. Six different gait types were identified by MCGHEE 1968 in periodic gaits, as shown on the left in Figure 1.1. If the robot shifts its center of mass during transition phases, the gait is intermittent; if not, it is continuous. Additionally, gaits can be characterized as spinning, turning, and straight crawling, their amount of crab angle, and the applicable terrain. The body workspace is defined as the motion space of the floating base when all four foot positions are fixed, as shown in Figure 1.2 (a). The robot can then be modeled as having spherical joints at each foot, connecting it to the ground (GONZALEZ DE SANTOS et al. 2006, SONG et al. 2015). The foot space describes the possible motion space of the feet relative to each other when the base is fixed (Figure 1.2 (b)). It is the same as the foot distance space that was used in previous work (GAISSER 2024).

Both for the body and foot space, their dimensionality is key to understanding the capabilities of reduced DoF quadrupeds. The body space always has twelve dimensions less than the system's total number of DoF because of the three additional floor constraints on each leg. The foot space has the dimension of the number of independent DoF of the feet without considering Rigid Body Motion (RBM). Six dimensions are necessary for each foot to be positioned relative to the other in 3D space, allowing omnidirectional locomotion. With four, only unidirectional crawling is possible within the quasi-static assumption.

A more general definition of a combined workspace is proposed. It portrays the intersection of the body space and constrained foot space, which depends on the number of stance feet. They are related to each other through the kinematics. Importantly, it tracks the combined dimensions of the body and the feet when n_f feet are positioned on the ground and describes the system's total DoF when modeling ground contacts as spherical joints. For $n_f = 4$ it resembles the body workspace (Figure 1.2 (a)), which has DoF_b dimensions. If three foot positions are fixed, the dimensions of the constrained workspace are increased to $DoF_b + (DoF_l - 3)$ (Figure 1.2 (c)). If two are on the floor, it has $DoF_b + (DoF_l - 1) + 1$ (Figure 1.2 (d)). Only one dimension is constrained by the two stance feet, and one additional DoF is present due to the rigid body rotation around the stance feet. With one stance foot $DoF_b + DoF_l + 3$ and with zero $DoF_b + DoF_l + 6$ dimensions are present in the combined space. With the available active DoF, the robot can selectively control dimensions in the foot or body

space. When each actuator is connected to multiple legs, both spaces are coupled. Moving any actuator affects both the foot space and the location of the CoM. Analyzing the body space for an uncoupled eight-DoF quadruped with $n_f = 3$ was done, for example, by SONG et al. 2015.

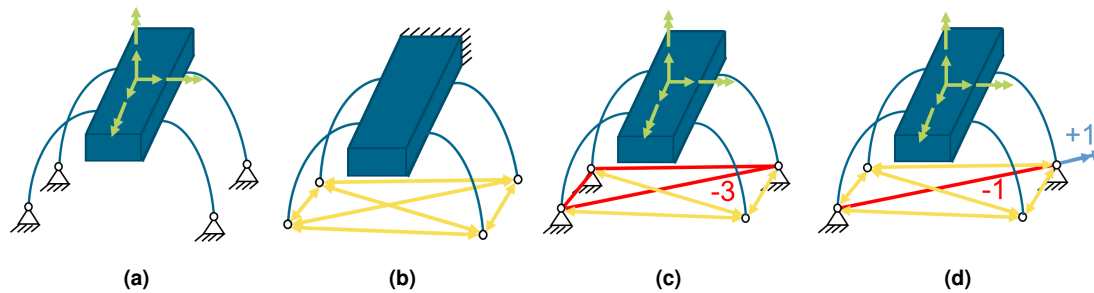


Figure 1.2: (a) Body space (b) Foot space (c) Combined space with $n_f = 3$ (d) Combined space with $n_f = 2$

1.1.2 Quadrupeds

Quadrupeds are robots with four legs. The most common approach is to use twelve actuated DoF, three for each leg, as implemented by KATZ et al. 2019 in the Mini Cheetah. This allows the robot to position and orient the floating base relative to the floor at all times due to the six DoF body workspace. Additionally, all feet can be positioned freely relative to each other, requiring an additional six DoF in the foot space. More than twelve internal DoF, like those present in Raibert's Quadruped (RAIBERT 1986) and Bert from DLR (SEIDEL et al. 2020), add additional redundancies to the spaces. Several attempts were made to design quadrupeds with fewer actuators to reduce the complexity and cost. There are designs with nine, eight, six, four, and three DoF, as shown in Table 1.1. With each reduction, these robots lose some ability to control the body and foot space. Two methods are applied to reduce the actuator count. Either DoF are fully removed or actuated passively. A third option is to exploit singularities, which apply to a whole region of the combined workspace.

Removing DoF decreases the capabilities of either the body or foot space and, therefore, the combined workspace. When the legs are coupled, like implemented in designs from Yoneda (YONEDA et al. 2000) or King (KING 2022), the control architecture can decide in which space they want to use the available DoF. To keep some capabilities, many designs use passive joints. These can then be constrained through ground contact, assuming the spherical joint connection. Additionally, passive elements like springs can influence the equilibrium in the quasi-static regime. All designs that passively control DoF rely on the floor to have suitable properties. On low friction or uneven surfaces, their control structure does not assert any DoF to manipulate the forces that are applied to the ground, which can lead to slipping or other uncontrollable behavior.

The singularity in a design by Kaneko (KANEKO et al. 1986), adds a permanent DoF to the z-direction of the body by keeping the actuated DoF on each leg parallel in all configurations. Usually, singularities only occur in specific configurations, like in Buehler's design (BUEHLER et al. 1998), when all joint angles are identical. The additional DoF from these configuration-dependant singularities are not included in Table 1.1.

Two previous designs with six actuated DoF are shown in Table 1.1. King (KING 2022) uses three additional passive DoF, which are defined by the constraints in the foot space in the case $n_f \leq 3$. When crawling, the mechanism is exactly constrained, similar to the design by

Source	DoF actuated	DoF passive	Dimensions of body WS	Dimensions of foot WS	internal DoF without RBM
RAIBERT 1986	12	4*	6	6	16
KATZ et al. 2019	12	0	6	6	12
ZHANG et al. 2015 YONEDA 2007	9	0	3	6	9
SEIDEL et al. 2020	8	8*	6	4	16
KANNER et al. 2014	8	4*	6	6	12
BONEY et al. 2022 SONG et al. 2015	8	0	2	6	8
KING 2022	6	3	3	6	9
KANEKO et al. 1986	6	2	2 + 1**	6	8
GAISSER 2024	6	0	0	6	6
YONEDA et al. 2000	5	2	1	6	7
BUEHLER et al. 1998	4	0	0	4	4
YONEDA et al. 2000	3	2	1	4	5

* passive DoF are constrained by springs.

** permanent singularity in all possible configuration in z-direction adds one DoF, due to perpendicular DoF. Many of the other robots also have singularities, but only in some configurations.

Table 1.1: Selection of quadrupeds with different numbers of actuated and passive DoF and their availability for controlling foot and body workspace dimensions

Kanner (KANNER et al. 2014). In cases $n_f < 3$, at least two of the three DoF are unconstrained in addition to the rigid body motions, increasing the problems of underactuation present in all quadrupeds with point contacts in these cases. Also, the ground forces cannot be controlled due to the passive DoF. Kaneko et al. (KANEKO et al. 1986) proposed a design with two passive DoF besides six partially coupled actuators. One actuator controls each leg separately, and one influences only the body space with a rotating mass attached to the floating base. Only the extension of the floating base couples the body and foot space when crawling. With this design, the DoF in the body workspace allows positioning the CoM in the correct support polygon in all configurations, while the others are used in the foot space.

All other concepts except Scout by Buhler (BUEHLER et al. 1998) have at least one DoF to manipulate the body workspace. Yoneda (YONEDA et al. 2000) stated: "In order to prepare for complicated locomotion tasks, e.g., dynamic trotting and step climbing, the body workspace is necessary to plan the motion of CoM. " Scout manages to walk, run, climb steps, and manipulate the CoM in a zero-dimensional body workspace by using dynamic movements. In a later prototype, he added four linear springs to the legs, similar to Raibert's quadruped (RAIBERT 1986), to enhance its running capabilities. Considering these springs as passive DoF, the robot would actually have a small four-dimensional body workspace, which can be actuated by tensioning the springs through ground interactions, but it is likely insignificantly small when quasi-statically trying to shift the CoM.

1.2 Goals

To the author's knowledge, the proposed design, shown in Figure 4.1, is the first quadruped with six actuated DoF that is fully constrained without considering floor interactions, meaning it has no additional passive DoF. The goal of this work is to show that with a zero-dimensional body workspace, stable crawling gaits are feasible. This objective incorporates defining a suitable space to search locomotion patterns in, finding parameters that can describe a variety of gaits, determining a strategy to efficiently explore this parameter space, and assessing it concerning stable and reliable motion as well as self-intersections and joint limits. Finally, the goal is to test the validity of the results both in simulation and in real-world conditions. For that, suitable software needs to be developed, an appropriate simulation environment needs to be created, and hardware needs to be developed for testing. The goal is to design and build a robot that allows for verifying the used models.

1.3 Design of the Robot

The design is based on the optimized kinematic developed in previous work (GAISSER 2024). Through the optimization, an increase in the robot's foot space and rotational symmetry was obtained. The design allows all four feet to position themselves in all three dimensions, hence having a six-dimensional foot space with only six DoF. This is achieved by coupling the motion of each motor to two distinct legs. The quadruped has 31 bodies joined by six revolute (1 DoF), 24 universal (2 DoF), and 16 spherical joints (3 DoF). Applying Grübler's formula results in $6(31 - 1 - 46) + (6 * 1 + 24 * 2 + 16 * 3) = 6\text{DoF}$, without considering the ground interactions as constraints. In a crawling gait, either three or four feet touch the ground. Since they are designed spherical, the small contact area can be modeled as additional spherical joints. Three contact points yield nine additional DoF, three additional joints, and one additional body, which reduce the available DoF in the combined workspace with $n_l = 3$ to $6(32 - 1 - 49) + (6 * 1 + 24 * 2 + 19 * 3) = 3\text{DoF}$. This means three of the six motors are constrained by the condition to keep the stance feet at the same position, where they can influence the forces applied to the ground so that these stay in their friction cones. The other three motors are used to control both the position of the moving foot and the CoM. When also the fourth foot touches the ground, all six DoF and, therefore, all motor positions are constrained. Grübler's Formula results in $6(32 - 1 - 49) + (6 * 1 + 24 * 2 + 20 * 3) = 0\text{DoF}$ assuming all constrains are independent. With the full kinematic structure constrained also the CoM is defined. This case occurs during the crawling sequence when all feet touch the ground. All DoF are defined by the foot space, and the body space collapses to a single point. No intermittent gait cycles are possible.

All six revolute joints are attached to the floating base of the robot and are each actuated by a servo motor. As shown in Figure 1.3, the robot has four-way rotational symmetry along the z-axis. A leg assembly consists of two motor links, four leg links, one top link, and one leg. The foot is the endpoint touching the floor. The leg assemblies are connected at the motor links. To have a fully defined structure, the leg links connect the leg with a universal joint, the motor links with a spherical joint, and the top links use universal joints for both ends. As described in section 2.7, all 24 universal joints are replaced by spherical joints in the final design. This adds 24 DoF, allowing all passive links to rotate around their major axis until the joint limits are reached. These additional DoF do not influence the position of the feet, and their orientation is not important for crawling.

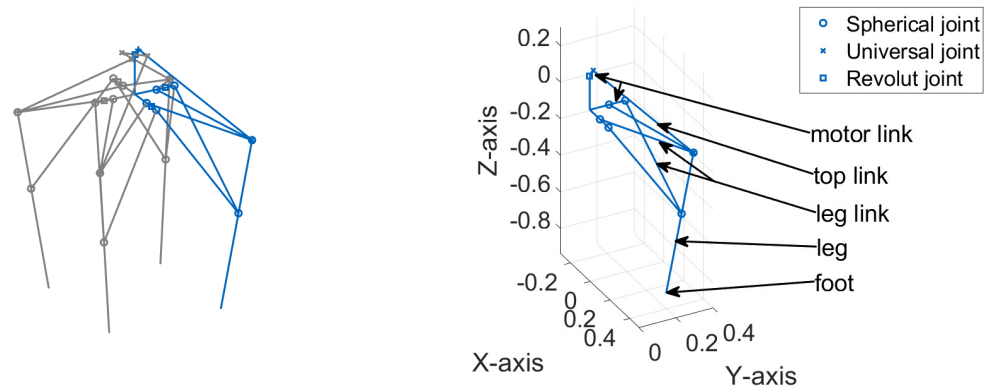


Figure 1.3: The structure of the robot (left). One of the four leg assemblies is marked in blue. The structure of a leg assembly (right). The joints are drawn as circles, crosses, and squares, and the links as lines. The scale is non-dimensionalized and shows the relative proportions (GAISSER 2024).

The used reference frames are shown in Figure 1.4. The body frame of reference is defined relative to the floating base of the robot (blue). The z-axis coincides with the symmetry axis of the base, and the x- and y-axis lie in the plane of rotation of the lower motor links, with the x-axis pointing towards one of the motor links. The ground-related coordinate system (green) defines the floor plane. Its z-axis is normal to the plane and points against the gravitational vector. The robot walks towards the x-axis, so foot 1 is always the front left foot and has positive coordinates in both x- and y-direction. When $n_f = 3$, a constrained frame (orange) is used. It has the origin at the stance foot opposite the stepping foot; all three stance feet lie on the xy-plane, and the x-axis points toward the angle bisector of the two other stance feet.

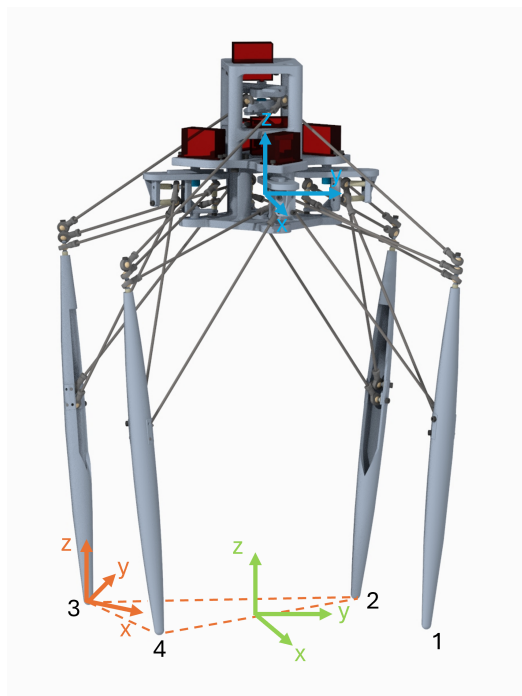


Figure 1.4: Shown are the coordinate systems used in this work. The body frame is shown in blue, the green one is fixed at the ground, and the orange frame is used to describe the constrained foot space. The dotted lines mark the distances between the stance feet.

Chapter 2

Method Selection

The proposed process of identifying feasible gait patterns and validating them involves several key steps. The applicable methods of each are discussed and selected in this chapter. First, the motion space is defined by finding gait parameters that can describe the studied gaits and bounding them, followed by the use of specific metrics to assess the feasibility of the gait patterns. Methods for path generation are then discussed based on the chosen gait parameters, and how to derive the required motor positions from the foot trajectories. Methods to verify the motor trajectories and evaluate path metrics against expected performance are presented. Lastly, constructing a physical robot relies on design methodologies and mechatronic considerations essential for validating these gaits in real-world conditions. The chosen methods of each step are marked in gray in the comparison tables below.

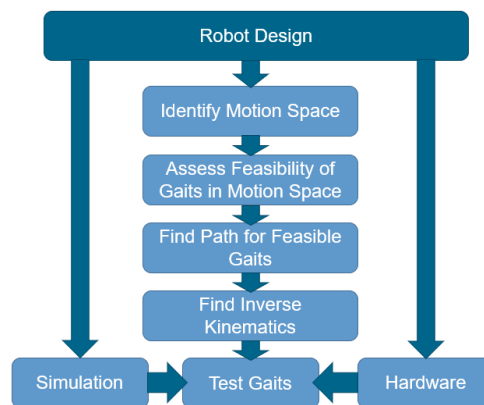


Figure 2.1: The main structure of the work. After defining the motion space, the feasibility of different gaits is assessed, paths for them are generated, translated to motor commands via inverse kinematics, and then tested on the simulation and hardware.

2.1 Identify Motion Space

For exploring quadrupedal locomotion, both static and dynamic approaches, as well as model-based and optimization-based strategies, can be used. Given the robot's highly complex kinematics and dynamics, a black-box optimization approach could be considered. However, integrating system-specific insights, such as symmetries and periodic motion, can help refine and reduce parameters, potentially enhancing model capabilities. For instance, incorporating

techniques like Central Pattern Generators (CPGs), which can exploit periodicity could yield efficient movement capabilities through a blend of physics-based and data-driven insights. To later advance towards a highly dynamic and adaptable control strategy, the thesis sets the foundation with an in-depth understanding of quasi-static, periodic crawling gaits. These findings provide a foundational understanding of the system, upon which more advanced control algorithms can build. The primary focus of this thesis is on open-loop crawling, with a view toward extensions into dynamic adaptability and optimization strategies.



Figure 2.2: Relationship between active joint angle space and foot space. The feasibility assessment is simpler when creating the trajectories in the parameterized foot space.

Generating quasi-static crawling motion by varying parameters in the active joint angle space was tried. This was not well suited for crawling since the constraints in the foot space are very restrictive due to the fixed position of the stance feet, while in the joint space, only the joint limits need to be held. The joint space representation might be more suited for dynamic movement and is highly dependent on the accuracy of the simulation, in which the parameters are adjusted. Translating quasi-static motion to the real robot by searching in the parameterized foot space was found more promising and gave more insight into the model-specific constraints. The restriction of the joint space can be addressed by solving the inverse kinematics (Figure 2.2).

Method	Advantage	Disadvantage
Parameterized joint space	Simple to tune Few parameters	Sensitive to simulation errors Restrictive foot space
Parameterized foot space	Translates well to real-world Model insights	Many different parameters

Table 2.1: Advantages and disadvantages of parameterizing the active joint angle space and the foot space.

2.2 Assessing feasible gaits in parameterized foot space

Assessing feasibility implies finding appropriate gait designs in a given search. The parameter space approach, described by Merlet (MERLET 2006) for coupled kinematics, attempts to find a set of solutions that fulfill all requirements regarding stability and workspace. In this solution space, secondary constraints like stability margins can be addressed.

To reduce the search space of possible solutions, a flat ground is assumed and the periodicity of the motion is set to one gait cycle, meaning each foot moves exactly once before the same joint configuration is reached. To move forward during the stepping motion each foot must, therefore, move the same amount and in the same direction as shown in Figure 2.3. This reduces the parameters to the two components of the 2D step vector, gait type, and initial foot configuration, as well as trajectory specifics, particularly the lift-phase height. Increasing the periodicity increases the number of parameters. When considering each step individually, the possibilities of finding stable gaits become even larger. But also, the search space becomes too large for a parameter space approach, and deadlocks can occur, where no solution to the next step can be found (GONZALEZ DE SANTOS et al. 2006).

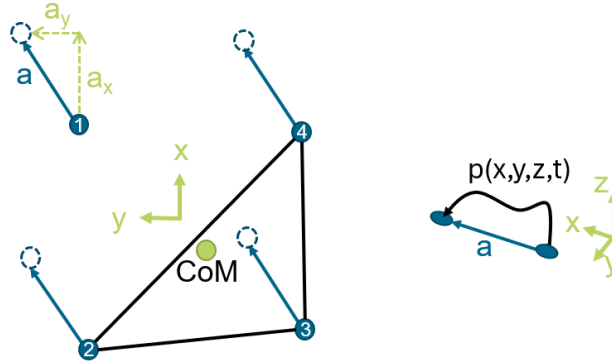


Figure 2.3: Parameterized gait assuming one gait cycle. Each step can be described by the step vector a , the gait type and the path p .

Method	Advantage	Disadvantage
Periodic gait	Less parameters	Additional Constraints
Free gait	More freedom in trajectory design Higher stability margins possible	More Parameters Potential deadlocks
Trial and error	Fast	Cannot find all configurations
Mathematical assessment	Exact	Complex subdivided motion space
Sampling	Efficient	No exact solution
Closest edge stability margin	Simple	no information on scale
Tipping energy stability margin	Estimation of the possibility of tipping	more computation
Absolute joint limit	Simple Bound Less prone to errors to avoid servo damage	Restrictive
Conditional joint limit	Less restrictive	Complex to determine conditional statements

Table 2.2: Advantages and disadvantages of assessment methods.

Bounding these parameters involved exploiting insights into the geometry, particularly regarding symmetry. Also, a workspace estimation using a simplified model from previous work (GAISSER 2024) was used to gain insights into the most promising search region.

A rigorous search is conducted in the bounded parameter space. The continuous configuration space is discretized and a grid-based sampling method is applied. The sample assessment is split into three parts, first focussing on the highly constrained transition point configurations, where the body workspace collapses to a single point. Then information on the gait type and crawling direction are included. This way infeasible solutions can be excluded before investigating the full stepping trajectories. During the stepping phases, the available DoF of the combined space increase as shown in Section 1.1. A mathematically exact formulation of the stability regions was not conducted, because the discontinuous state-based integral formulation of the combined workspace did not reveal any practical use cases for the path generation.

Self-collisions of the robot are addressed by restricting the range of motion of each motor so that, independent of the motion of the other motors, collisions are avoided. Stable gaits are searched, where no joint violation occurs.

2.3 Sampling in configuration space

The approach requires sampling configurations corresponding to the transition points, where all feet's z-components are zero in the ground frame. Both the x- and y-directions of all four feet can vary, leaving eight variables.

The foot space considers only the relative distances between the feet and not the RBM, which makes it indifferent to translations and rotations of the robot. A distance space can be considered to sample in, as done in previous work in 3D (GAISSER 2024). Considering planar configurations, this requires only four variables, which describe the four distances between the feet, shown in Figure 2.4 (left) in blue. These can be randomly sampled or found with an equidistant grid search.

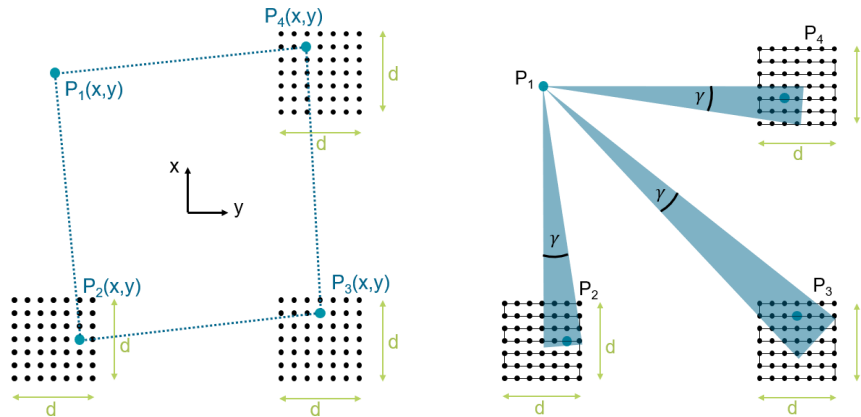


Figure 2.4: Shown on the left is the distance space with four variables (blue dotted lines) and grid space with six variables (black dots). On the right is a visualization showing that small angle changes γ relative to the stepping direction are included in the 6D-grid space.

Increasing the number of variables by two has several advantages over this four-dimensional space. Three equidistant grids can be defined with these six variables, as shown in Figure 2.4 in black. The fourth foot can be fixed due to the translational indifference of configuration space and the other feet can vary on their grid. The first advantage is, that the indexing for retrieving the precomputed information later is more intuitive on an equidistant grid compared to the 4D-distance space. Also, all four transition points, which must be evaluated during a periodic straight crawling gait differ by a fixed length vector a . This means for any step that lands back on a grid point, the configuration can be exactly found in the precomputed dataset. In the distance space, an interpolation between the evaluation of the closest samples would need to be performed, which might not always be unique and introduces complexity. Finally, since the information on the orientation of the configuration is contained in the sample, it includes small differences in the crab angle in the solution space. This is shown in Figure 2.4 on the right. To reduce complexity, this simpler 6D grid search was performed (Figure 2.4).

One idea to enlarge the search space of the 6D grid approach is to exploit additional symmetries of the robot. If one of the feet leaves the domain, the rotated or mirrored configuration

might still be found in the grid domain. The additional complexity this poses to the sampling evaluation was also not found fruitful to implement.

Method	Advantage	Disadvantage
Sampling in distance space	Only four dimensions	Less intuitive to index samples May require interpolation between sample evaluations
Sampling in grid space	Small crab angles captured in samples Exact evaluation in periodic gaits possible	Six dimensions necessary Increased computational load

Table 2.3: Advantages and disadvantages of sampling methods.

2.4 Path generation

The stepping path is chosen rectangular, consisting of a lift, traversing and lowering phase of equal duration. A smoothing function allows for soft accelerations around corners. In addition to the direction and size of the step, the path only needs the height as an additional parameter. To address different angles of the step vector and spinning gaits, coordinate transformations are used to transform the directional motion accordingly. Even though more advanced paths involving bezier curves or trigonometric functions can improve locomotion performance, they were disregarded since they do not add to the goal of finding feasible gait dynamics and often need additional parameters.

Method	Advantage	Disadvantage
Curved Path	Smooth motion	More parameters, which are not necessary for assessing feasibility
Rectangular Path	Only height as additional parameters	Jerkier motion

Table 2.4: Advantages and disadvantages of Paths.

2.5 Inverse kinematics

No analytic solution was found for the coupled inverse kinematics. Libraries like PyKDL (OROCOS 2024) or Pinocchio (CARPENTIER et al. 2024) exist, which can compute the joint angles with a control-inspired Closed-Loop Inverse Kinematics (CLIK) approach. Since the simulation was performed in Mujoco (DEEPMIND 2024), using the same toolbox for computing the inverse kinematics was found to be the simplest, although a dynamic update step using an advanced version of a Quadratic Programming (QP) optimization is used, which might increase computation time, and dynamic effects need to be considered. On the flip side, the influence of gravity and stiffness can be included in the inverse kinematic, which might lead to more accurate joint state estimation. Also, additional soft constraints to address singular configurations and assembly modes are easy to include.

Method	Advantage	Disadvantage
CLIK	Faster	No stiffness and gravitational effects
QP-optimization	Soft constraints can be included to address singularities No additional toolbox necessary	Slower Dynamic effects need to be mitigated

Table 2.5: Advantages and disadvantages of CLIK vs QP-optimization solver.

2.6 Test motor trajectories

The motor trajectories generated by the Inverse Kinematics (IK) need to be tested. This is done both in simulation for fast feedback and on the physical hardware to verify the real-world applicability. The simulation is performed in Mujoco. Compared to similar physics engines like Gazebo it offers better contact physics and offers more capabilities in defining the robot. Compared to other XML formats like URDF, the .mjcf format has useful functions to close kinematic chains and attach spherical joints. For the hardware test, a prototype is designed and built. Both straight walking and spinning gait patterns are tested on a flat plane.

Method	Advantage	Disadvantage
Simulation	Fast iteration possible Assess feasibility of gait independent of hardware specs	Model inaccuracies can not be captured
Hardware	Prove real-world applicability of gaits	Slower More Expensive

Table 2.6: Advantages and disadvantages of simulation and hardware testing.

2.7 Mechanical Design

To design and build the hardware on which feasible gaits are tested, several methods were used. The model is first designed in Creo (PTC 2022), using a motion skeleton to define the kinematic dependencies. Due to the physical dimensions of the parts, several deviations from the optimization model used in previous work (GAISSER 2024) had to be made. 3D printing in combination with standardized parts is used to reduce cost and simplify the manufacturing process. The motors, motor controller, and microcontroller are repurposed from a previous prototype (GAISSER 2024). This way additional cost was avoided.

Key design methodologies included reducing the deformations under load and increasing the stiffness while keeping the weight down. Also, self-collisions are attempted to be reduced to mitigate a compromised workspace. The most sensitive parameters found through a sensitivity analysis (GAISSER 2024) should be kept as close as possible to the model and asymmetries are avoided when possible. Also, the number of distinct parts is reduced, and screws should be reachable in the assembled state when possible.

Chapter 3

Gait Generation

In this chapter, the selected methods are applied to create gaits that can be executed by the robot. After defining the requirements and constraints for feasibility, a search space is defined in which feasible gaits are searched. This includes finding the parameters that describe the periodic gait space and their boundaries space. Next, a three-stage evaluation strategy is described to assess different gaits inside the motion space regarding stability and generate paths for them. Lastly, the foot trajectories need to be transferred to the motion of the motors via inverse kinematics (IK).

3.1 Constraints and Requirements for Feasibility in Crawling Gaits

Several requirements and constraints for the body space and the foot space are proposed in this chapter. First, the constraints regarding stable crawling with reduced DoF quadruped are defined (Table 3.1). Then, the requirements for the used robot are defined (Table 3.2).

Constraints	Description
$CoM \in SP_f$ at $t = t_{LO,f}$	At liftoff of foot f CoM is in corresponding Support Polygon (SP)
$CoM \in SP_f$ at $t = t_{TD,f}$	At touchdown of foot f CoM is in corresponding SP
$\dot{p}(f, t) = 0 \quad \forall t \in T / \{t_{TP}\}$ $\forall f \in f_{stance}$	During stepping phases, the stance feet retain relative distances
$z(f_{step}, t) > h_{floor} \quad \forall t \in T / \{t_{TP}\}$ $CoM \in SP_{f_{step}}$	During stepping phases, the stepping foot f_{step} is above the ground and the CoM is in the right SP

Table 3.1: The constraints concerning stable crawling, including the stability at transition points and stepping phases the constraints concerning the foot space, including the conditions on the velocities of stance feet, and the height of the stepping foot.

For crawling the constraints shown in Table 3.1 are identified. At each point one foot must be able to move. To move a foot, the CoM must be in the SP formed by the stance feet. These stance feet should have no velocity relative to the ground. During stepping the swing foot should clear the ground. At the transition points, to CoM must be positioned so that the next stepping foot can lift off the ground. Assuming also a soft touch down of the previous foot would mean $CoM_{TD,f} \in SP_f$ and $CoM_{LO,f+1} \in SP_{f+1}$, from which it follows that:

$$CoM_{TD,f} = CoM_{LO,f+1} \in SP_f \cap SP_{f+1} \quad (3.1)$$

At the transition points, the CoM would need to be in the SP of both feet. While neighboring feet share a common stability region, opposing feet's support polygons only share a single edge (Figure 3.1), since the zero-dimensional body space does not allow for intermittent gaits. This means a consecutive movement of opposing legs can only be achieved with a stability margin of zero or allowing tipping before the touchdown. This tipping along the long diagonal is allowed in this work for stable walking, despite violating the quasi-static stability constraint.

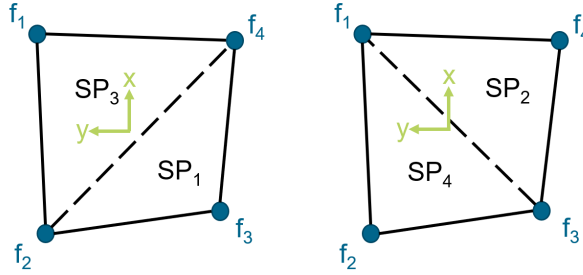


Figure 3.1: Definition of the feet indices and corresponding SP. The long diagonals are dotted and mark the intersection of opposing SP.

The requirements for this work are defined in Table 3.2. The used methods (Chapter 2) assume a flat plane, so at the transition points between steps, all four feet are required to be in the xy-plane and during stepping, the stepping foot must have a positive z-component. The design of the robot, which is explained in Chapter 4, requires the active joints to have specific limits shown in Table 3.2, and the average stability margin should be above 0.02m to be robust against slight disturbances.

Requirements	Priority	Description
$z(l_{step}, t) > 0 \forall t \in T / \{t_{TP}\}$	high	During stepping phases, the stepping foot is above the xy-plane
$z(l, t) = 0 \forall t = t_{TP} \text{ and } l = 1 \dots 4$	high	At transition points, all feet are in the same plane
$\Phi_{1-4} \in [-30^\circ, 30^\circ] \forall t \in T$ $\Phi_{5,6} \in [-45^\circ, 15^\circ] \forall t \in T$	high	Joint angle limits are held for motor j during full gait cycle
$\frac{1}{T} \int_0^T SM(t) dt > 0.02m$	medium	Average stability margin is above a threshold of 0.02m

Table 3.2: The requirements for the specific design choices and assumptions used in this work, including the average stability margin during the full gait cycle, staying inside the workspace limits set by the joint angles and the conditions on the height of the stepping foot.

3.2 Boundaries of the Search Space

In this chapter, the parameters and their boundaries are defined, which make up the search space, in which the feasibility of gaits is assessed.

By constraining the periodicity of the gait to one step cycle of length T and the path of the stepping foot to a rectangular path with a fixed height of 3cm, the search space can be defined with nine variables. They consist of the x- and y- component of the step vector, the gait type, and the six dimensions to define the initial configuration (Table 3.3). Additional parameters are needed to quantify the discretization of the trajectory in time and space.

Parameters	Boundaries	Description
a_x	[-0.12m,0.12m]	x-component of the step vector a
a_y	[-0.12m,0.12m]	y-component of the step vector a
g	[[1, 2, 3, 4], [1, 4, 2, 3], [1, 3, 2, 4], [1, 3, 4, 2], [1, 2, 4, 3], [1, 4, 3, 2]]	gait type
x_2	[-0.05m,-0.17m]	foot 2's initial position in x
y_2	[0.05m,0.17m]	foot 2's initial position in y
x_3	[-0.05m,-0.17m]	foot 3's initial position in x
y_3	[-0.05m,-0.17m]	foot 3's initial position in y
x_4	[0.05m,0.17m]	foot 4's initial position in x
y_4	[-0.05m,-0.17m]	foot 4's initial position in y
h	0.03m	stepping height
p_1	(0.11m,0.11m)	foot point 1
l_{av}	0.22m	average width of the robot
n	9	number of discretization in configuration grid
T_{min}	10s	minimal period of one gait cycle
Δt_{max}	0.001s	maximum time step size

Table 3.3: The boundaries of parameters including the step vector a , gait type g , initial position and path height h used for the parameter search and parameters used for path discretization in time and space.

The workspace is visualized in Figure 3.2 to find suitable bounds for the parameters shown in Table 3.3. Also, an average width l_{av} of the robot is defined, which helps bounding the search space.

The visualization of the constrained workspace (Figure 3.2 (left)) is done by sampling randomly in the joint space, using the same voxel representation as in the previous work (GAISSER 2024). The reachable voxels of one of the feet use an analytic Forward Kinematics (FK) estimation. In the previous work (GAISSER 2024), a projection of the 6D workspace is visualized, in which all six stance feet's distances are represented. A hyperplane in this space is shown in blue in Figure 3.2 (left), complying with the reduced joint limits and a fixed distance of the stance feet. The resulting workspace approximates the motion range of a moving foot for a given set of fixed stance feet in the constrained frame of reference. The red plane with $z = 0$ shows the reachable voxels for the transition point configurations.

The average width l_{av} of the robot is used as the distance between adjacent stance feet in the constrained workspace in Figure 3.2. This width is defined as the distance neighboring feet

have when the joint angles are in their middle position relative to their bounds. While for the lower motors, this is the same as in the ideal model, due to the asymmetric bound of the upper motors, they are shifted by -15° . This results in an average width of around 0.22m.

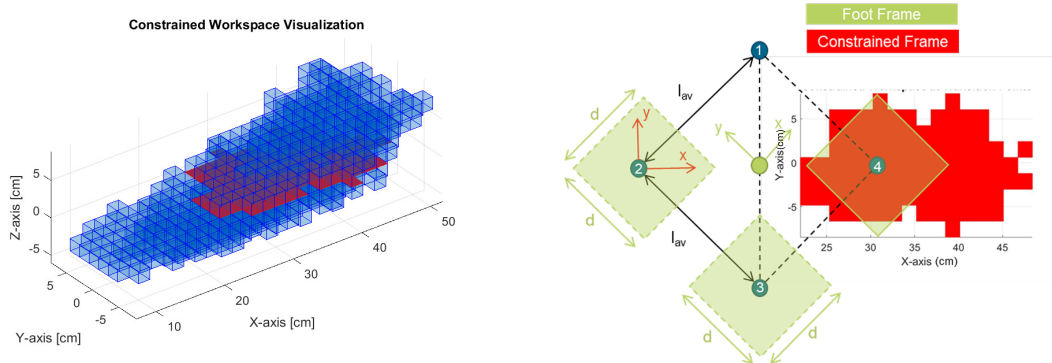


Figure 3.2: Shown on the left is the 3D representation of the constrained workspace estimation using the idealized model from (GAISSER 2024). The dimensions relate to the constrained frame on reference in [cm]. The red faces are in the xy-plane, corresponding to transition point configurations. On the right is the overlap between the sampling grid (green squares) and the workspace (red) visualized. Adjacent stance feet are average width l_{av} apart from each other.

Based on insights from Figure 3.2 all parameters are bounded as follows:

The centers of the grids, visualized as green squared in Figure 3.2, are the average width apart from each other. In this way, it is assumed that the most evaluated configurations are inside the workspace of the feet.

In the constrained frame, the largest motion is possible in the x-direction. Since all feet have the same workspace, each rotated by 90° , a step performed by all feet needs to also be inside the workspace when it is rotated by 90° . Therefore, the biggest steps should be possible with the y-component a_y of the step vector being zero in the foot coordinate system. From the workspace estimation, a length $\|a\|$ of at most 14cm of the step vector might be possible with $a_y = 0$. However, due to the varying position of the stance feet during a gait cycle, the upper limit is expected to be smaller.

The range d of grid points is then chosen symmetrically around the average width, ensuring that many configurations within the workspace are tested, as indicated in Figure 3.2, but the grid density does not get too small. Nine points per grid dimension were used for sampling in the configuration space (section 3.3.1), so a range of 0.12m with a distance between points of 0.015m was chosen as a good compromise. This also limits the range of step vector a . Both the x- and y-coordinates of foot 1 are fixed as explained in section 2.1 and set to half of the average width.

The height h is chosen to be 3cm. While no rigorous grid sampling was performed, different heights were tested, and a compromise between workspace, ground clearance, and stability margin was found. In general, a larger step height leads to more workspace violations, but better ground clearance and larger stability margins. As Figure 3.2 indicates, much higher stepping heights are not feasible for the used geometry.

As defined by MCGHEE 1968, six different gait types g exist. The four crossing gaits [1,3,2,4], [1,3,4,2], [1,2,4,3], and [1,4,3,2] differ only by the direction of the step vector a , as shown in Figure 3.3. By allowing negative values for the step vector parameters a_x and a_y and defining the front left foot as foot 1, the gait types can be reduced to the three bold ones in Table 3.3.

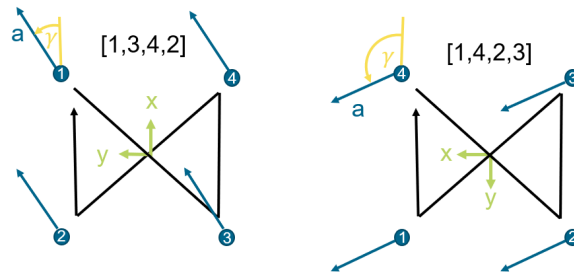


Figure 3.3: The front left foot is always foot defined as 1. The step vector always has a positive x-component, which is larger than the y-component. For angles γ outside the range of $[-45, 45]$, the crossing gaits change type and the coordinate system is rotated to fit the notation.

3.3 Gait Assessment using the Parameter Space Approach

This section describes how the gaits are assessed using a parameter space approach suggested by MERLET 2006 for coupled kinematics. The assessment can be divided into three parts as shown in Figure 3.4. First, all configurations inside the bounds of the grid, as defined in section 3.2, are pre-evaluated (Section 3.3.1). Next, the parameter space is sampled at the transition points (Section 3.3.2), and finally, the foot trajectories during a full gait cycle are assessed (Section 3.3.3).

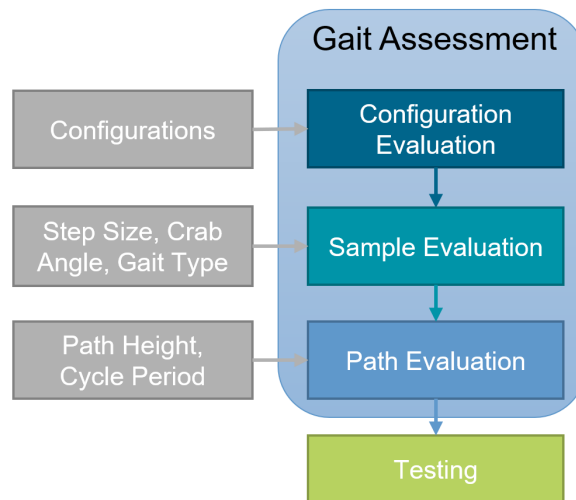


Figure 3.4: Visualization of separation of the gait assessment into three parts. The separation reduces the feasible solutions step by step so that more computationally intense evaluations only need to be done for good candidates.

Without this separation, all samples need to be evaluated along the full gait cycle. This poses a computational challenge, as a requirement (section 3.2) could be violated at any moment during the cycle. In MuJoCo (DEEPMIND 2024), the continuous path is divided into discrete time steps Δt . At each time step, the dynamic equations are solved iteratively as explained in section 3.4.

By dividing the assessment into three separate parts and first focusing only on the transition points, many configurations can already be excluded since they violate the requirements there. The computationally intense path evaluation during the stepping phases then only needs to be done for a small set of candidate samples.

Initially, the path is assumed to fulfill stability as long as the start and end points are stable. This means that only the four transition points between steps are evaluated for each sample. By pre-evaluating a set of configurations, the sampling evaluation can use the configuration results without having to compute the IK. All samples use the same configuration space at the transition points, so this configuration evaluation only needs to be done once.

3.3.1 Configuration Evaluation

The first step of the three gait assessment steps (Figure 3.4), namely the pre-evaluation of the transition point configurations is described in this chapter. The flow chart is shown in Figure 3.5, and the corresponding algorithm 1 below.

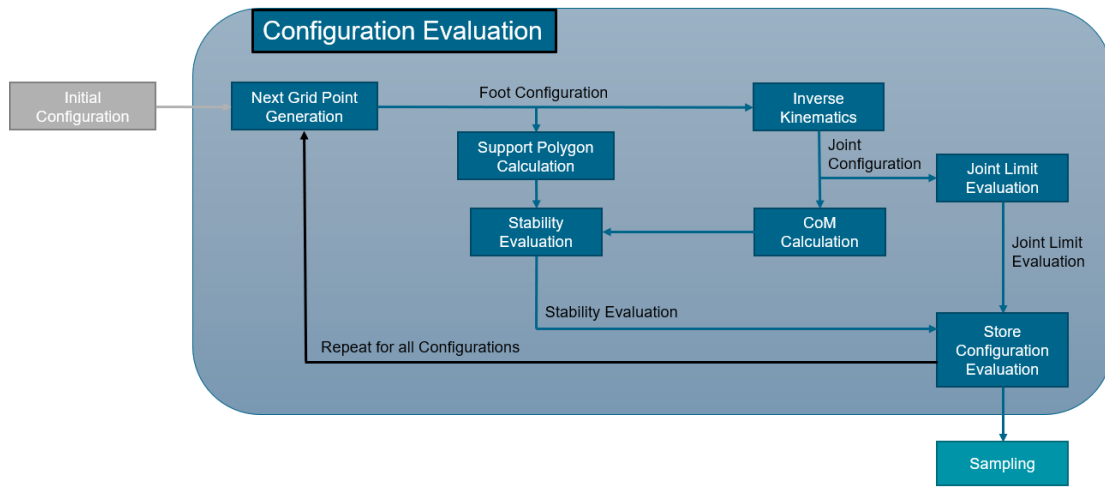


Figure 3.5: Flow chart of the configuration evaluation.

Algorithm 1 Configuration Evaluation

```

for configuration = 1, ..., 96 do
  targetFootPos = generateSnakePath(grid)
  while base ≠ settled & targetFootPos ≠ reached do
    mj_step()
    jointAngles, CoMproj = inverseKinematics(targetFootPos)
    if any(|jointAngles| > jointAngleLimit) then
      jointLimitExceeded = True
    for f = 1, ..., 4 do
      SP = [FootPos((f + 1)%4), FootPos((f + 2)%4), FootPos((f + 3)%4)]
      inSP = isPointInPolygon(SP, CoMproj)
      if inSP then
        SM = computeSM(SP, CoMproj)
  return jointLimitsExceeded, inSPs, SMs
  
```

The algorithm 1 outputs five binary values for each configuration, which are stored for sampling. The first one indicates whether any motor joint limit is violated in the configuration, and the other four values indicate whether the CoM is in the corresponding SP (Figure 3.6). Since the configuration grid is described by six parameters, each with nine discretization steps (section 3.2), 9⁶ configurations are represented by the grids.

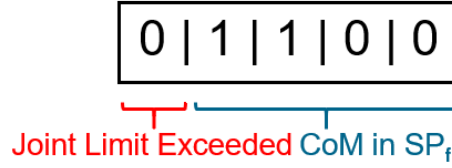


Figure 3.6: Information stored in precomputation for each configuration.

To obtain the five values, the inverse kinematics need to be solved for each sample. As described in section 3.4 the inverse kinematic is solved using MuJoCo as a solver. It provides a shorter convergence time and faster settling dynamics when the sampling points are closer together. Points are, therefore, sampled in a snake-like pattern so that consecutive configurations always differ in one foot by a single grid length. This is done by following a snake-like path and reversing the direction when the end is reached, as shown in Figure 3.7.

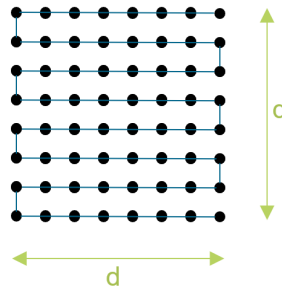


Figure 3.7: Shows the path the simulation takes when sampling the configurations. The snake-like path is followed back and forth until all configurations are evaluated.

The configuration's information is stored in a list. Its index is generated by referencing the x- and y-coordinates of each foot in the grid and mapping them to an index in the range of $[0, 8] \in \mathbb{N}$. These indices i are then weighted and added together as shown in equation 3.2, so that each configuration has a unique configuration index I , at which the configuration is stored in the list.

$$I = i_{x_2} * n^5 + i_{y_2} * n^4 + i_{x_3} * n^3 + i_{y_3} * n^2 + i_{x_4} * n + i_{y_4} \in [0, n^6[, \text{ with } n = 9 \quad (3.2)$$

In total, 9^6 configurations are calculated. To ensure the solver has converged, the solver iterates until the error of the foot positions relative to the target is kept below a threshold of 1mm. A second error is tracked to ensure the dynamic motion has settled. For that, the position change of the base between update steps is tracked. When the deviation remains below 1mm over the past ten iterations, the configuration is defined as settled. Each point takes around 30 steps to reach these convergence criteria. With nine points per grid dimension, 531.441 configurations must be evaluated, requiring around three hours to compute on the used hardware (Table 3.4). This was chosen as a good compromise to have meaningful results and a manageable computation time.

Figure 3.8 shows examples of the 2D capability map when all other feet are in the center location of their grid. The red regions represent the unreachable zones due to the joint limits, the others the location of the CoM with respect to the support polygons. On the left is the map of foot 3, and on the right, the map of foot 4 is shown. All five possible evaluation states are present in the exemplary map.

Property	Specification
Processor	Intel Core i7-1185G7
Processor Speed	3 GHz
RAM	16 GB
Python version	3.12
MuJoCo version	2.3.7

Table 3.4: Hardware specifications including the processor, its speed, the memory, and the used version of Python and MuJoCo.

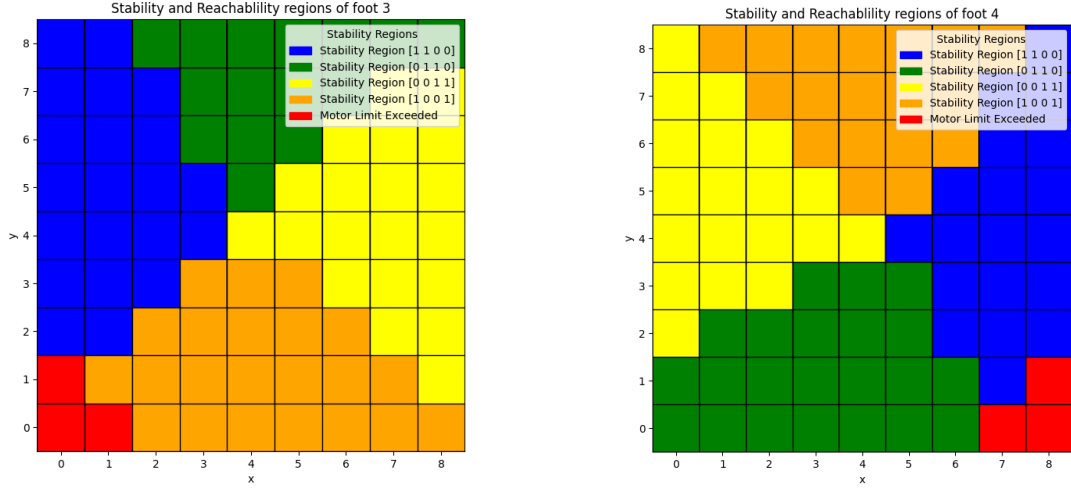


Figure 3.8: The Feasibility map of foot 3 (left) and foot 4 (right). When all other feet are in the center location of their grids. The x-axis points towards the right. Shown are the evaluations when moving the respective foot around in the grid.

3.3.2 Sample Evaluation

Using the information of the pre-computed configuration, the transition points during one gait cycle can be evaluated for a given set of parameters. The flow chart is shown in Figure 3.9 and the corresponding algorithm 2 below. It takes a set of parameters and outputs an assessment regarding the feasibility at the transition points, using the pre-evaluated configurations.

If a step vector's x- and y-component lie on the grid, all four transition point configurations can be found in the pre-evaluated set. A step in the x-direction of foot $f \in [2, 3, 4]$ by m_x grid increments means the new index is shifted by $s_x = m_x * n^{9-2f}$ compared to the index I (equation 3.2) of the previous configuration, and a step by m_y increments in y direction is shifted by $s_y = m_y * n^{8-2f}$.

$$I_{new}(f) = \begin{cases} I_{old} + s_x(f) + s_y(f) & \text{if } f \in [2, 3, 4] \\ I_{old} - \sum_{i=2}^4 (s_x(i) + s_y(i)) & \text{if } f = 1 \end{cases} \quad (3.3)$$

The first foot always lies on the same point, exploiting the translational invariance (section 2.1) of the grid domain. The configuration occurring after foot one has moved can be evaluated by shifting it so that the foot returns to its initial position, as shown in Figure 3.10. This

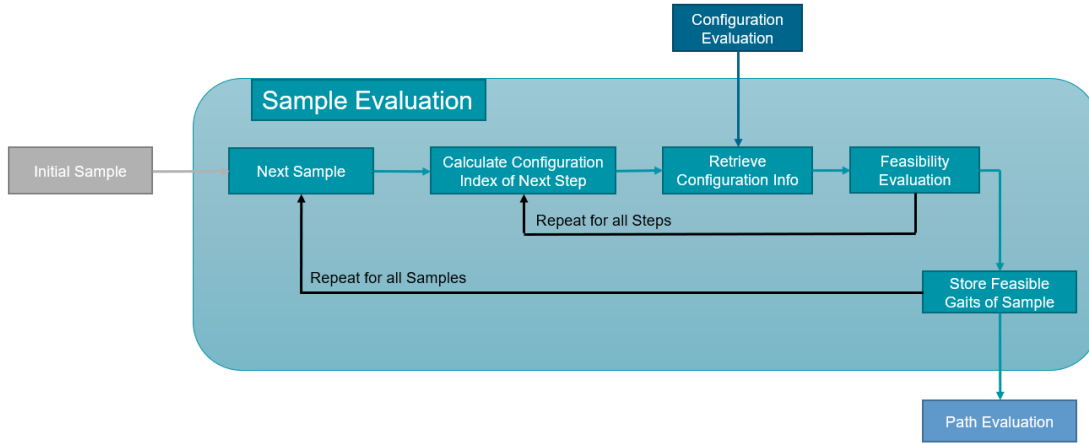


Figure 3.9: Flow chart of the sampling evaluation.

Algorithm 2 Sampling

```

for variationsOf( $\alpha$ , crabAngle, gait) do
  for configuration = 1, ..., 96 do
    configurationIndices = getTransitionPointIndices(stepSize, crabAngle, gait)
    for  $i = 1, \dots, 4$  do
      jointLimitExceeded, inSP, SM = retrieveConfigInfo(configurationIndices( $i$ ))
    if any(jointLimitExceeded) then
      feasibility = False
    for  $i = 1, \dots, 4$  do
      if any(inSP(gait( $i$ )) = 0) then
        feasibility = False
  return feasibility( $\alpha$ , crabAngle, gait, configuration)

```

means the new configuration for $f = 1$ has all other vectors shifted by the negative amount (Equation 3.3). The next foot in the gait cycle is determined by g .

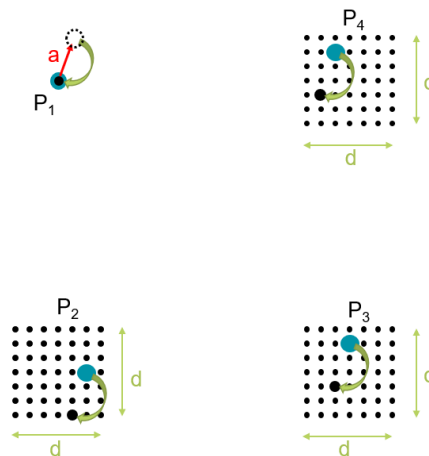


Figure 3.10: After the first foot takes a step of size a , the configuration is shifted back onto point P_1 .

Each of the four configurations corresponding to the transition points needs to lie inside the grid and fulfill the stability and joint angle requirements for the parameter set to be feasible for quasi-static crawling. The sample is considered stable when tipping only occurs along the

long diagonals as described in section 3.2. The CoM is positioned so that the next foot in the gait cycle can be lifted.

3.3.3 Path Evaluation

Once a stable set of transition configurations is found, a corresponding path can be generated, which connects them (Figure 3.11). The 50 most promising paths were chosen by ranking the solutions from sampling by the stability margins at the transition points.

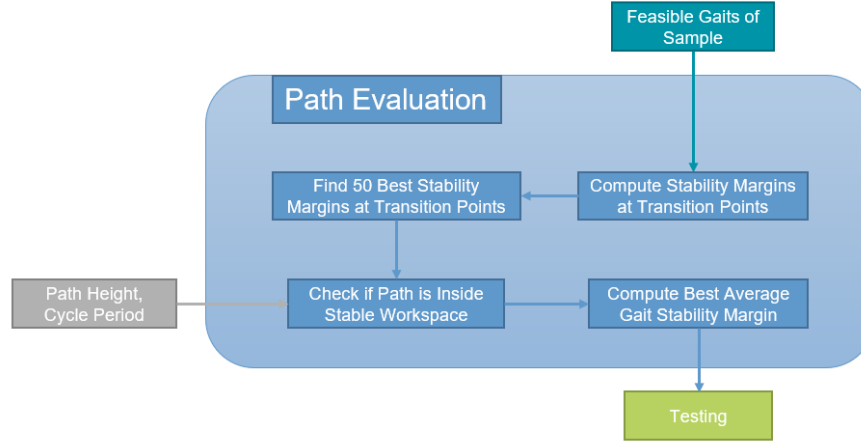


Figure 3.11: Flow chart of the path evaluation.

The path is imposed on the motion capture points in MuJoCo and one full gait cycle is simulated. After every time step Δt , a dynamic update step is performed, as described in section 3.4, to get to the next target position along the path. If any joint limit is violated or the path does traverse an unstable region at any time step, the tested configuration is marked as "no feasible path found" in the list of feasible samples. This does not mean that there exists no path that fulfills the requirement, but that the tried attempt failed. There likely is a more complex trajectory that avoids the unstable or self-colliding configurations. The trajectory p_f of the stepping foot f_s consists of lifting traversing and lowering the foot and is calculated as shown in equation (3.4), where the duration of the step T_s is 1/4 of the gait period T :

$$p_f([x, y, z], t) = \begin{cases} [ca_x, ca_y, ht] & \text{if } 0 < t < \frac{1}{3}T_s \\ [ca_x + a_x t, ca_y + a_y t, h] & \text{if } \frac{1}{3}T_s < t < \frac{2}{3}T_s, \text{ with } c = \lfloor t/T \rfloor \\ [(1+c)a_x, (1+c)a_y, h(1-t)] & \text{if } \frac{2}{3}T_s < t < T_s \end{cases} \quad (3.4)$$

The time for lifting, traversing, and lowering the foot are all chosen as 1/3 of T_s . The starting time of each step is then shifted according to the stepping position in the gait type g , and the starting location is shifted in the stepping direction by the number of step cycles c , which are already completed.

To smoothen the motion of the feet, a sinusoidal smoothing function modifies the linear time t of length $\Delta t_d = 1/3T_s$, to make the motion close to a sharp corner in the path trajectory slower, and speed up the time in between turns, as shown in equation 3.5.

$$t_{smooth} = \frac{1}{2} \left(1 - \cos\left(\frac{t}{\Delta t_d} \pi\right) \right) \quad (3.5)$$

3.4 Inverse Kinematics

In this section, it is described how the joint angles are calculated by defining the trajectory of the feet. It is shown how MuJoCo solves the coupled inverse kinematics. The joint angles are uniquely defined from the position of the feet due to the zero-dimensional body workspace, except for some singular configurations (Chapter 3.4.1) and assembly modes (Chapter 3.4.2). These are addressed by using constraints shown in Table 3.5.

Constraint	Type	Parameters	Usage
Motion capture points	"weld"	solref=[0.002 1] solimp=[0.9 0.99 0.001 0.1 2]	Chapter 3.4.1 Chapter 3.4.2
Motor limits $[-\pi/2, \pi/2]$	"limit"	stiffness=100 margin=0.001	Chapter 3.4.2
Spherical Joints	"connect"	solref=[0.002 1] solimp=[0.99 0.999 0.001 0.1 2]	Chapter 3.4.3

Table 3.5: Tunable parameters for constraints of the Mujoco simulation (DEEPMIND 2024)

3.4.1 Singularities

Singularities occur in configurations where DoF become linearly dependent on each other (MERLET 2006). Type 2 singularities, allowing motion of the feet, while the joint angles are fixed, were prevented in the preceding workspace optimization (GAISSER 2024). Type 1 singularities were not avoided, though, since they do not reduce the foot space and do not lead to controllability issues. The same is true for type 3 singularities.

While type 3 singularities are not present in the configuration space, by replacing the universal joints with spherical joints, an uncontrolled rotation of parts of each leg assembly occurs in all configurations. Similar to type 3 singularities, they do not affect the controlled DoF of the end effector. In this case, these are the position of the feet. Still, these rotations can lead to instabilities of the simulation, if the motion becomes too fast. The problem was addressed by setting small enough time steps.

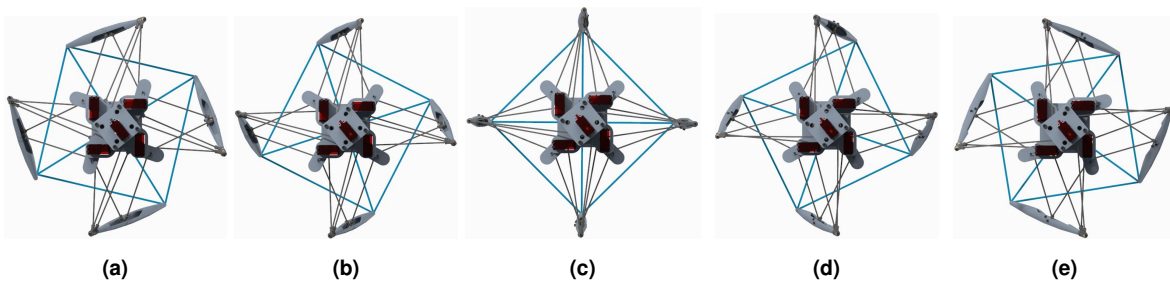


Figure 3.12: Top view of five different type 1 singular configurations with the same distances in the foot space (blue lines), for lower motor angles of 30° (a), 15° (b), 0° (c), -15° (d), and -30° (e)

If the feet are positioned so that the robot has rotational symmetry, a type 1 dependency occurs, which lets the robot twist around its z-axis as shown in Figure 3.12. Also, for configurations close to the singularity, oscillations occur due to the badly conditioned inverse kinematics. These are addressed by replacing the "connect" constraints with "weld" equality

constraints between the motion capture points and the feet. The parameters used for the MuJoCo settings are shown in Table 3.5. They try to keep the feet's orientation upright by inducing correction moments at the feet. These unphysical moments might lead to deformations and errors in the joint angles, so it is important that the stiffness of the robot is high compared to the applied moments as elaborated below. The alternative of applying stabilization moments at the active joints was avoided as it generates errors directly at the joints and cannot be compensated by the structure.

3.4.2 Assembly Modes

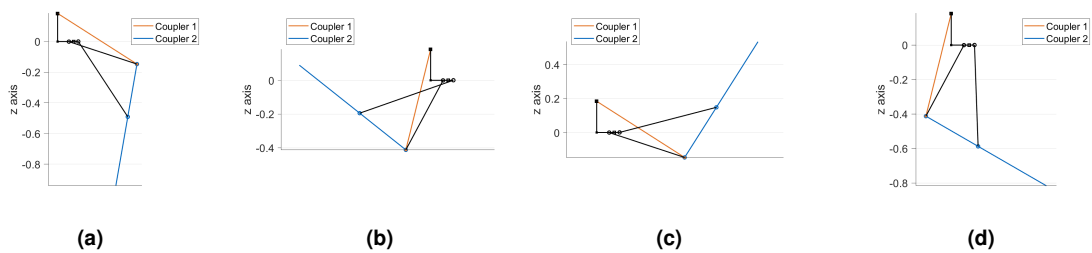


Figure 3.13: The four different assembly modes of a single leg assembly, where (a) is the used configuration (GAISSER 2024)

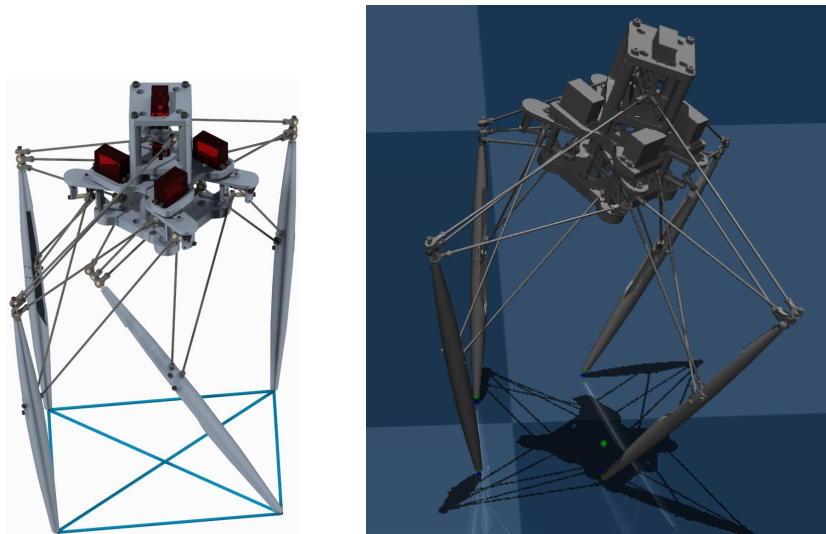


Figure 3.14: Shown are two error modes where the solver converges to the wrong assembly mode. The one on the left is prevented by using "weld" constraints at the feet, and the right by introducing limit constraint at the active joint angles.

Another problem when dealing with coupled kinematics is assembly modes. Each leg has four assembly modes, shown in Figure 3.13), and the solver converges to one of the 256 possible modes depending on the starting conditions. The assembly modes (c) and (d) of each leg never occur in practice, as they are too far away from any initial conditions in the foot space. Without addressing the problem, one error mode is for some legs to be in assembly mode (b), as shown in Figure 3.14 (left). This is avoided by the "weld" constraints, whose moments let the solver tend towards assembly mode (a). Another error mode is shown in Figure 3.14 (right). Here two of the motor joints violated the joint limits beyond a critical joint angle and are now stuck in this configuration. One way to avoid the problem is to always start with

the robot in its home position, with all active joint angles being zero. However, the faster convergence of neighboring points cannot be exploited then. The assembly mode issue in practice always occurs together with a violation of the joint limits, so it was opted to use soft constraints after the joint limit is exceeded by a critical amount. The limits are set to $[-\pi/2, \pi/2]$, with a stiffness of 100Nm and a margin of 0.001 (Table3.5).

3.4.3 Calculation using the QP-Optimization Method

In MuJoCo, kinematic coupling is done with soft equality constraints. Spherical joints, as present in the coupled chains, are conveniently simulated with the "connect" constraint, which induces a corrective force to keep the two points accelerating toward each other while the orientation is not constrained. These "connect" dependencies attach the leg links to the leg to close the kinematic chains at the spherical joints. With four "weld" constraints, the motion capture points are placed in the center of the spherical foot. This way, fewer errors will occur from the roll-off behavior. The "weld" equality also tries to align the orientations, which draws the robot towards the orientation of the initial configuration. Therefore, it is opted to start the simulation in a symmetric configuration to not impose asymmetric moments.

MuJoCo handles the equality constraints by solving a QP-optimization with the projected Gauss-Seidel method using Lagrange multipliers. While MuJoCo can include all sorts of physical interactions, the inverse kinematic can be solved using only these constraint forces f and some Newton mechanics. Joint limits, connect, and weld constraints are all captured in the framework of applying corrective forces under certain conditions. Also, ground contact, used in Section 5.1, can be simulated with them.

The accelerations of the active joint angles, which in the final step have to be integrated to get to the joint positions, obey Newton's law of mechanics:

$$\ddot{q} = M^{-1}(\tau - c + J^T f) \quad (3.6)$$

Here, f are the constraint forces acting on the system and are calculated as follows:

$$f = \arg \min_{\lambda} \frac{1}{2} \lambda^T (A + R) \lambda + \lambda^T (a_0 - a_{\text{ref}}) \quad (3.7)$$

subject to $\lambda \in \Omega$

where $A = JM^{-1}J^T$ tells the solver how the applied constraint forces f will influence the acceleration of the system within the constraint space Ω , and R is a regularization to obtain a convex problem.

An intuitive way to understand the constraint forces generated by the QP optimization (equation 3.7) is shown with the "connect" constraint. The other constraints follow similar approaches. Forces that close the distance between the two connected points A and B and are iteratively applied to the system (equation 3.6) until the error r is within tolerance:

$$r = P_A^{\text{glob}} - P_B^{\text{glob}} = T_A P_A^{\text{loc}} - T_B P_B^{\text{loc}} \stackrel{!}{=} 0 \quad (3.8)$$

This error r is fed into a tunable spring-damper system, which determines the acceleration $(a_0 - a_{\text{ref}})$ imposed to close the gap. A high impedance, which scales both spring and stiffness

constants, will produce higher accelerations, and higher constraint forces will be applied to the next iteration. This leads to stiffer constraints. The impedance can be set relative to the positional error r with the parameters in "solimp" as explained in the documentation (DEEPMIND 2024). Spring and stiffness can be tuned individually with "solref". A high impedance was used with values up to 0.999, as shown in Table 3.5, to model stiff spherical joints, and a critical damping ratio of 1 was used to mitigate oscillations. The high impedance and the over-constrained system can lead to large forces that can destabilize the simulation. Therefore, a small time step of 0.001s was necessary to simulate all 16 "connect" constraints of the robot and the additional 4 weld constraints at the feet. For the latter, an impedance value of at most 0.99 was chosen. With lower impedance values, the dynamics of moving in between configurations becomes more relevant. This leads to a longer settling time for the evaluation of the transition point configurations (Section 3.3.1) and the path evaluation (Section 3.3.3). Higher impedance values introduce larger moments at the feet. This leads to an error between the desired path (Section 3.3.3) and the actual path, which is investigated in (Section 5).

3.5 Results

In this section, the results of the feasibility assessment are presented. First, the transition point maps of a working gait cycle show the results obtained from the sampling. Then, statements for different parameter sets with respect to all possible configurations are made. The stability margin is investigated both for the transition points, as well as the full gait cycle, and the most robust configurations are shown.

3.5.1 Results from Sampling at the Transition Points

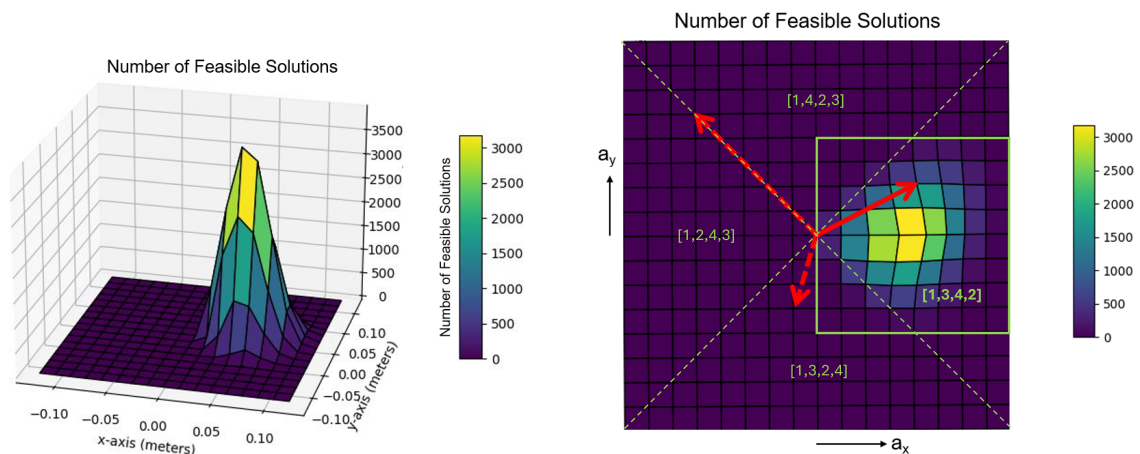


Figure 3.15: Shown the number of initial configurations that have feasible transition point configurations for the crossing gait-type $g=[1,3,4,2]$ different step vectors. By allowing the vector a to point in all directions, all four crossing gait types are covered. The borders, where the gait type changes, are marked by green dotted lines. The green square shows where the most feasible solutions lie in.

As shown in Figure 3.15, the gait type with the most feasible solutions is [1,3,4,2]. Out of all solutions, 95% have this gait type. In Figure 3.15 on the left, the number of solutions

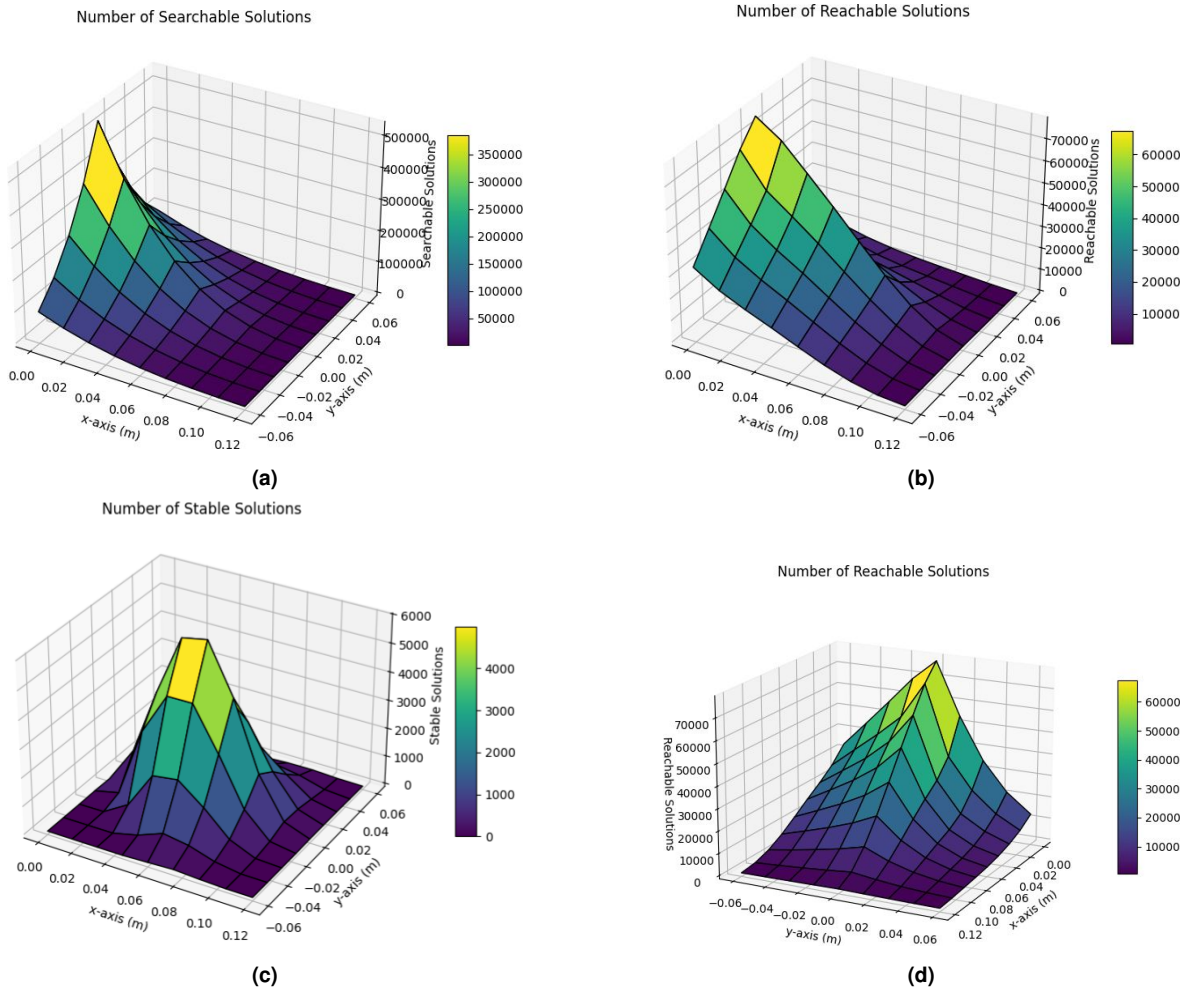


Figure 3.16: Figure (a) shows the number of searchable solutions, (b) the number of reachable solutions, (c) the number of stable solutions, and (d) the number of reachable solutions from a different angle to show the asymmetry. The assessments are done by sampling all four transition points of all configurations for the most promising gait parameter set, which is the green region in Figure 3.15 (right).

corresponding to the x - and y -values of the step vector is shown as the height of the bars. Larger x - and y -values than the grid's range d of 0.12m can not be analyzed, since either the configuration before or after the step is not on the grid. If the step vector does not point towards the x -direction, the gait type changes, as described in Section 3.2. Each grid point in Figure 3.15 corresponds to the x - and y -coordinate of a step vector for which all 9^6 possible initial configurations are evaluated. For each parameter set, the feasibility assessment is done for all four corresponding transition point configurations. Gait type $[1,3,2,4]$ makes up 3%, and type $[1,4,2,3]$ 2% of the feasible solutions, when separating them as shown in Figure 3.15 (right). All other gait types did not result in any feasible gaits. The most number of feasible configurations (3664) were obtained with parameters $a_x = 0.06\text{m}$, $a_y = 0\text{m}$, $g = [1,3,4,2]$. Figure 3.16 focuses on the green region in Figure 3.15 with $0\text{m} < x < 0.12\text{m}$ and $-0.06\text{m} < y < 0.06\text{m}$, where the most feasible solutions lie in. The number of searchable solutions (Figure 3.16 (a)) describes the number of initial configurations, where all transition configurations are in the grid throughout the gait cycle. The plot is symmetric, with the highest point at $a_x = a_y = 0\text{m}$. There, all four transition configurations are identical, so all 9^6 configurations can be assessed. The reachable solutions are not exactly symmetric, as shown in Figure 3.16 (b). Towards negative y components, more transition configurations lie inside

the workspace. Without stepping in any direction ($a_x = a_y = 0m$), the number of solutions represents the configurations inside the foot space. Of the 531,441 searchable solutions, 14% (74,331) are reachable there. The reachability is asymmetric towards negative y-components of the step vector (Figure 3.16 (d)). Around 60% of the stable solutions (Figure 3.16 (c)) are feasible (Figure 3.15). Compared to the stable solutions, the peak of the feasible solutions is shifted back from $a_x = 0.06m, a_y = 0m$ to $a_x = 0.045m, a_y = 0m$.

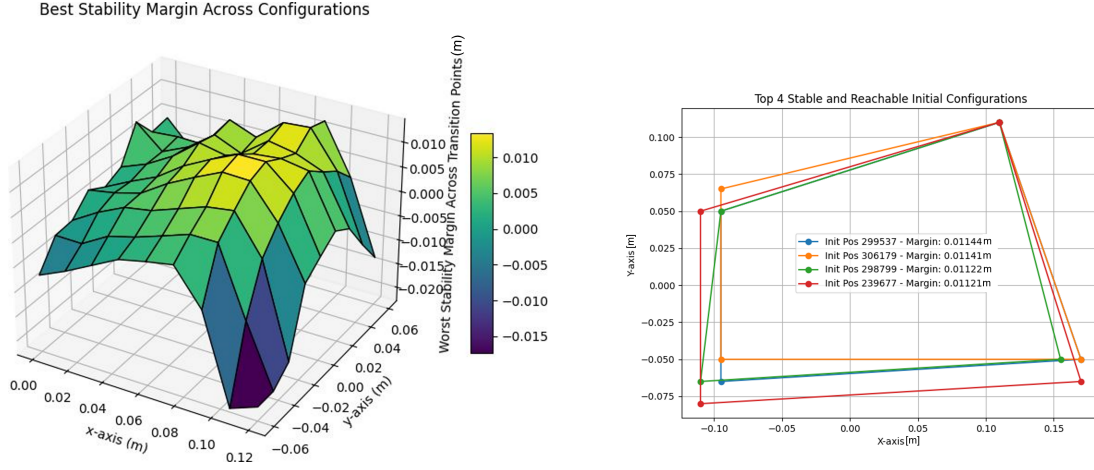


Figure 3.17: Shown on the left is the best transition point stability margin in [m] across all configurations for a specific parameter set on the grid. The transition point stability margin describes the lowest stability margin across all four transition points. Shown on the right are the four initial configurations, whose transition point stability margins are the highest with a step size of 0.06m in the x-direction.

The best stability margin of 0.0114m, considering only the transition points, can be achieved with $a_x = 0.06m, a_y = 0m, g = [1, 3, 4, 2]$, as shown in Figure 3.17 (left). The corresponding initial configuration is as follows:

$$\begin{pmatrix} f_1 \\ f_2 \\ f_3 \\ f_4 \end{pmatrix} = \begin{pmatrix} 0.11m & 0.11m \\ -0.095m & 0.065m \\ -0.095m & -0.065m \\ 0.17m & -0.05m \end{pmatrix} \quad (3.9)$$

This configuration (3.9) corresponds to the blue solution in Figure 3.17 (right). The four solutions with the best transition point stability margins are shown. They all have a similar shape.

The feasible set of transition point configurations is visualized in Figure 3.18 with gait parameters $a_x = 0.06m, a_y = 0m, g = [1, 3, 4, 2]$ and the initial configuration (3.9). After stepping with foot 1, the lifting condition of foot 3 is checked since it is the next step in the sequence. The CoM is inside the support polygon of foot 3, so it can lift off. Moving in the x-direction by four grid points corresponds to a step vector of $a = [0.06, 0, 0]$, reaching a new configuration after the second step. The grid shows the CoM is in SP 4. Foot 4 is able to lift off, and after step three, the CoM is inside SP 2. Finally, after step four, the initial configuration is reached again, where the first foot can be lifted (blue region). All four transition points are, therefore, suited for a stable gait.

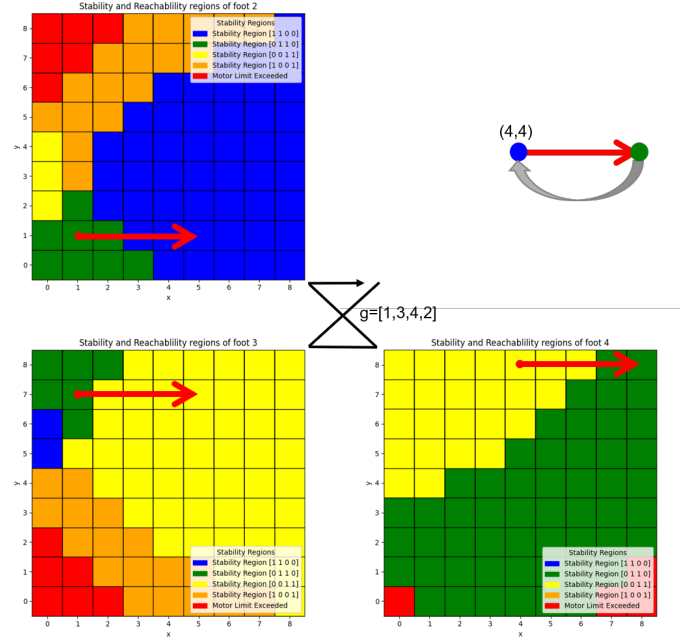


Figure 3.18: Shown are the feasibility maps on the sampling grid. The step vectors on each map indicate that for the given configuration (3.9), both the stability and reachability constraints are fulfilled at all four transition points.

3.5.2 Gait Results

The full gait is analyzed in this section, focusing on the most promising stepping parameters: $a_x = 0.06m$, $a_y = 0m$, $g = [1, 3, 4, 2]$

The 50 solutions with the best transition point stability margins for these parameters are analyzed regarding feasible paths. 12% of them violated the workspace with a stepping height of 0.03m, and 30% did not fulfill the requirement regarding the average stability margin being higher than 0.02m (Section 3.1).

Shown in Figure 3.19 is the parameter set with the best transition point stability margin shown in Figure 3.17 (blue trapezoid). It has an average stability margin of 0.024m across the full gait. Since it is a crossing gait, two tipping regions are present, as shown in Figure 3.19. They are both before the respective transition points, so the robot tips towards a stable configuration from where it can lift the next foot.

Shown in Figure 3.20 are the motor positions and CoM positions of three gait cycles for the highest found average stability margin of 0.034m. It has the following initial configuration:

$$\begin{pmatrix} f_1 \\ f_2 \\ f_3 \\ f_4 \end{pmatrix} = \begin{pmatrix} 0.11m & 0.11m \\ -0.065m & 0.11m \\ -0.11m & -0.08m \\ 0.11m & -0.095m \end{pmatrix} \quad (3.10)$$

The robot's CoM moves towards the stable SP in each step. At consecutive transition points ($\Delta t = 0, 5000, \dots, 60000$), the x position of the CoM always differs by around 1/4th of the step size. In total, it moves forward by 0.18m after reaching the initial position, which is 0.02m in front of the origin of the foot frame. The motor angles show periodic behavior and smooth

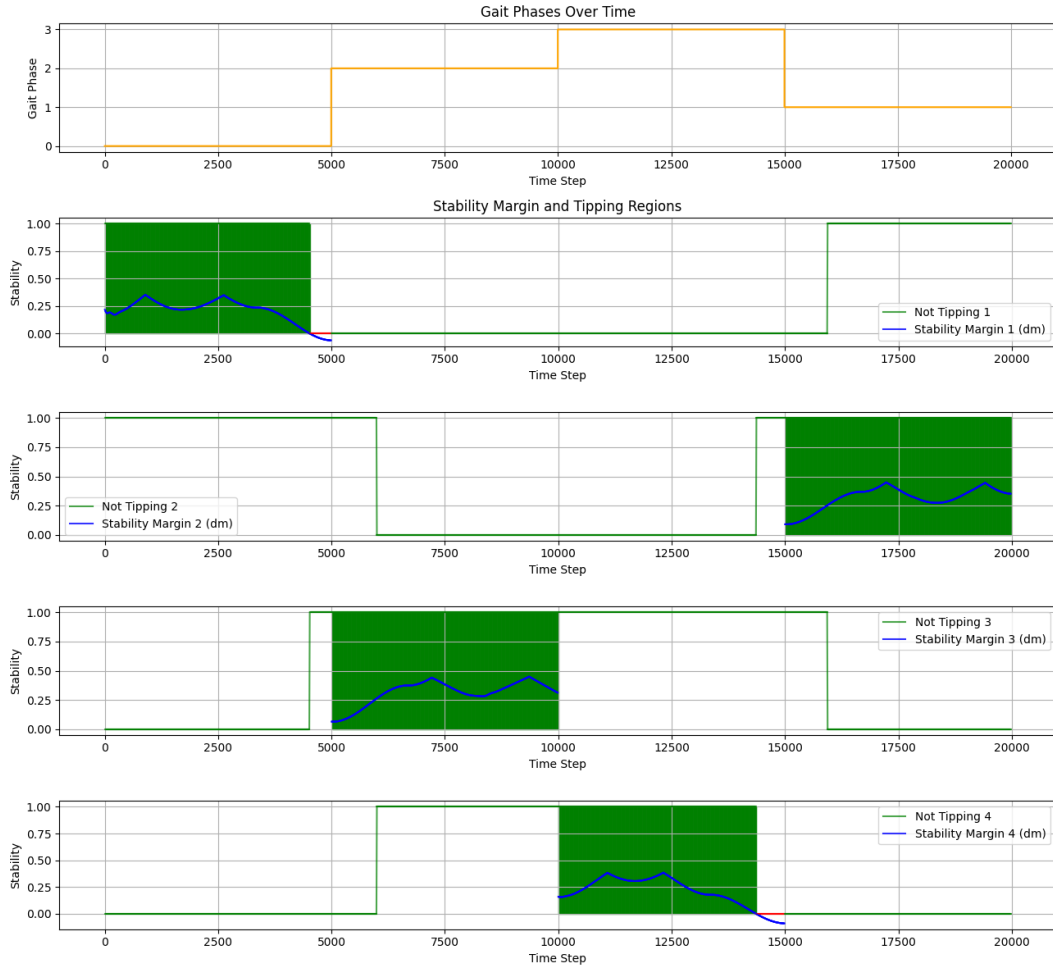


Figure 3.19: Shown is gait type (orange) and the stability margin (blue) during the full cycle for the initial configuration defined in equation (3.9). The green area is where the robot is statically stable and red lines mark the tipping regions.

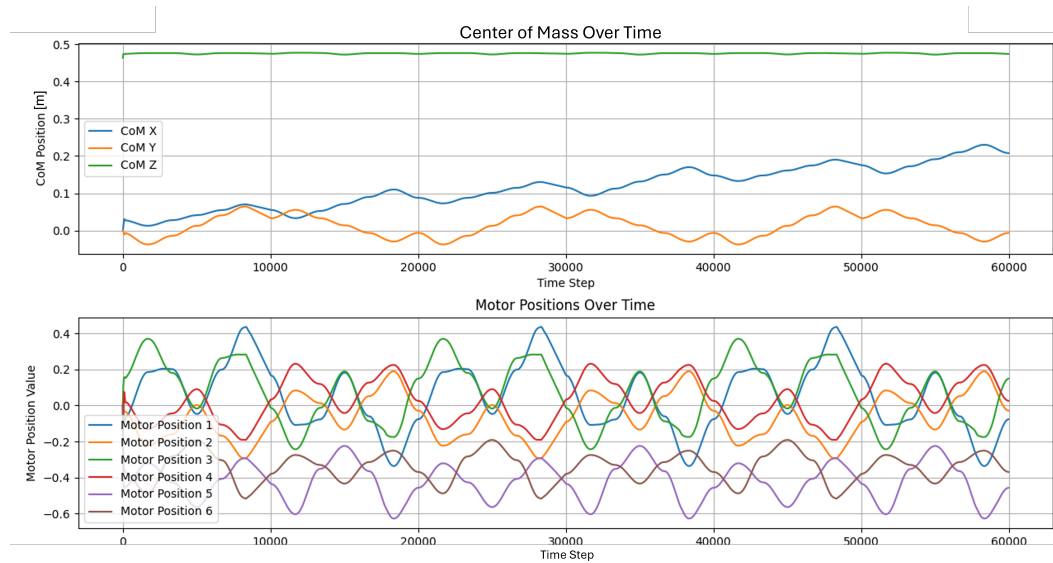


Figure 3.20: Shown is the position of the CoM in [m] and the joint angles in [rad] for three gait cycles. The x-component of the CoM moves forward by three step sizes.

trajectories. Both the lower motors (1-4) stay in their bounds of $[-0.52, 0.52]$, and the upper motors (5,6) in their bounds of $[-0.78, 0.26]$. The time series of the active joint angle data of one full gait cycle, which is generated through IK (Section 3.4), can be used to control the robot. The ability to reproduce the desired paths when crawling is tested in Section 5 for both configurations (3.9) and (3.10).

Chapter 4

Hardware

The section describes how the design process progressed from the idealized model used in the previous work to the finished quadruped. It shows which model assumptions had to be violated and which errors resulted from that.

4.1 Design Process

The section describes how the design process progressed from an idealized model (Figure 4.1 (a)) used in the previous work (GAISSER 2024), over the CAD model (Figure 4.1 (b)) to the finished prototype (Figure 4.1 (c)). Some key specifications of the robot are shown in Table 4.1. The part list and the technical drawing are shown in Appendix B.

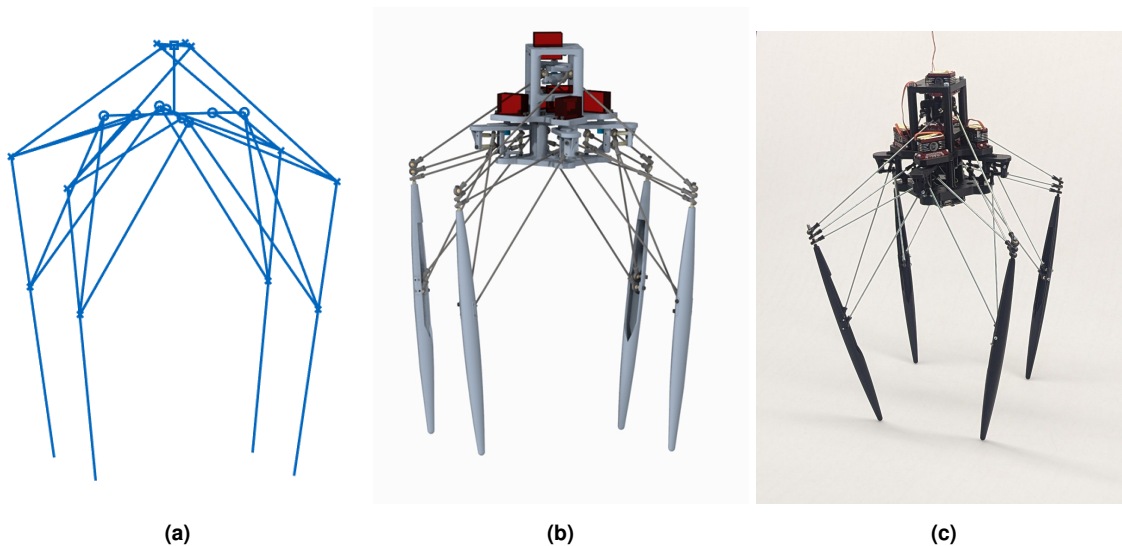


Figure 4.1: The three main stages along the mechanical design. (a) is the idealized model, used in previous work for optimization, and (b) is the Creo model, from which the physical prototype is built (c).

The previous work improved the robot's workspace by optimizing its geometry (GAISSER 2024). The model used is shown in Figure 4.1 (a). It is non-dimensionalized and assumes the kinematic can be described with spacial four-bars, which requires several spherical joints to share the same rotation point. Concepts that permit this joint configuration were, for example, developed by NASA and Hamlin (NASA 2022, HAMLIN and SANDERSON 1994). For

Quantity	Specification	Comment
Dimensions	w: 36mm h: 600mm	Width and height with 0 degree joint angles
Part Count	342	
3D printed parts	146	PLA with 20% infill
Standard parts	196	Joints, screws, threaded rods and inserts
Weight	1.49kg	
Cost estimate	800€	110.95€ per servo
Motor	6 BLS-H50B servos from Bluebird	
Motor dimensions	l: 40.5mm, w: 21mm, h: 38.5mm	Length, width, and height of a single motor
Motor weight	83g	
Motor torque	4Nm @ 5V	Used motor driver supplies 5V
Motor driver	Servo pHAT from SparkFun DEV-15316	I2C-bus with 1.6 kHz and 12 bit resolution
Microcontroller	Beaglebone Black	

Table 4.1: Some important Hardware specifications including the part count, weight, key dimensions and cost estimation.

the development of this robot, the rotation points are separated, though, to simplify the joint design. The separation can be seen in the CAD model in Figure 4.1 (b), which was created in the software Creo (PTC 2022). Additionally, the universal joints of the ideal model are replaced by spherical joints. It allows for a simpler design with fewer distinct parts and softens the requirements for the spherical joints. The feet's positions relative to the base, which are relevant for the kinematics, do not gain DoF by this modification, as explained in section 3.4.1. The spherical joints used (KBRM-03 from IGUS 1964) have a range of motion of 30 degrees in the off-plane direction (Figure 4.2 (left)). The rotation points of two joints must be placed at least 8mm apart from each other. One major design challenge was to position them in a way that does not reduce the robot's workspace and keeps the error between the ideal model (Figure 4.1 (a)) and the CAD model (b) small. This error was calculated in Creo using the average absolute differences of 660 configurations with an active joint angle range of $[-45^\circ, 45^\circ]$ (Figure 4.2 (right)).

The physical dimensions of the other components besides the spherical joints still lead to collisions in certain joint configurations, which reduces the workspace compared to the ideal model (Figure 4.1 (a)). Three collision modes are identified, which are shown in Figure 4.3. As hinted in section 2.1, collision is avoided by restricting the range of motion of the active joints to a fixed range independent of the other joint angles. As defined in section 3.1, with a range of $[-30^\circ, 30^\circ]$ of the lower four motors, no collisions occur. The worst found configuration for this collision type is shown in Figure 4.3 (a). The two collision types (b) and (c) in Figure 4.3 can be avoided with an asymmetric range of $[-45^\circ, 15^\circ]$ for the upper motors, which reduces the average width l_{av} of the robot to 22cm (Section 3.2). The constrained workspace, shown in Figure 4.4 is reduced by 65% compared to the wider range of $[-45^\circ, 45^\circ]$ for all joints, used in previous work for optimization (GAISSER 2024).

Both the absolute foot errors (Figure 4.2) and the reduced workspace (Figure 4.4), mean the kinematics must be solved using the more accurate joint configuration of the CAD model (Figure 4.1 (b)) and not the simplified one (Figure 4.1 (a)).

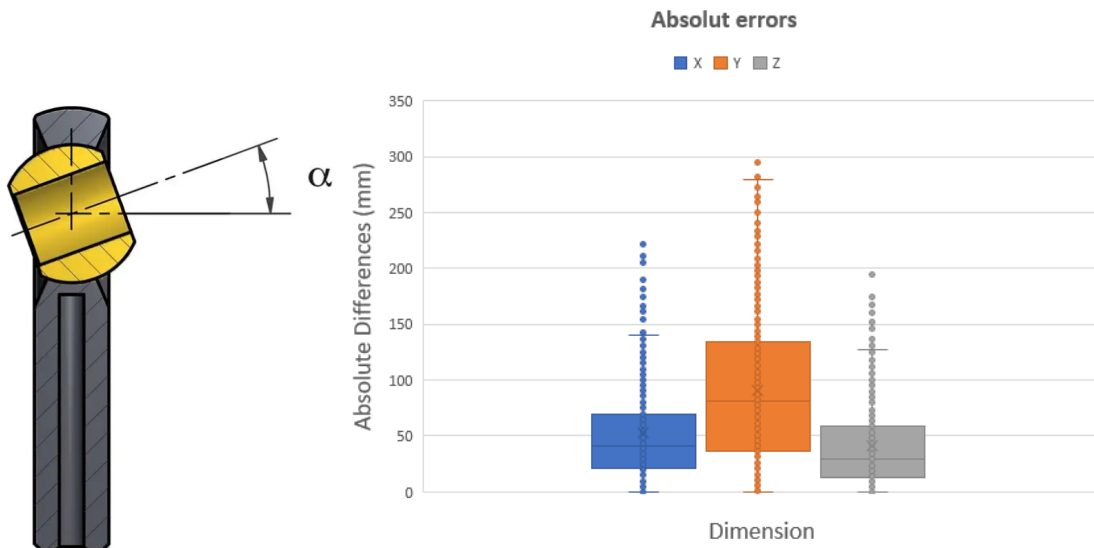


Figure 4.2: The range of motion α of the used spherical joint KBRM-03 from IGUS 1964, shown on the left is 30° , and two of them must be placed at least 8mm apart from each other. The resulting error distribution between the idealized and accurate model's foot position is shown on the right.

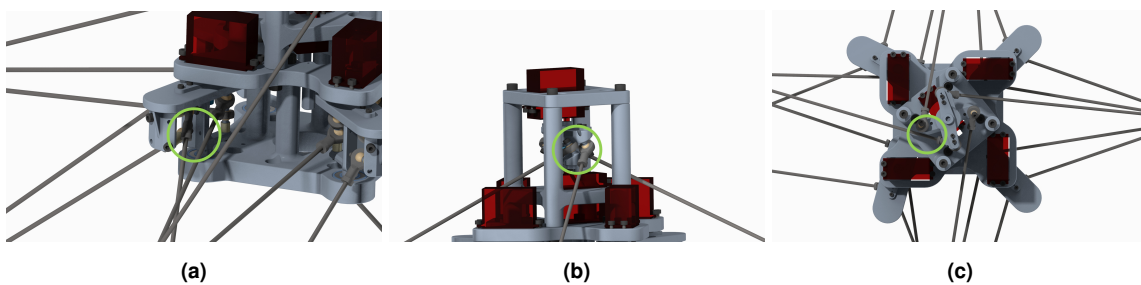


Figure 4.3: Collision configurations of lower motor link and leg links (a), neighboring top links (b), and upper motor link and top link (c).

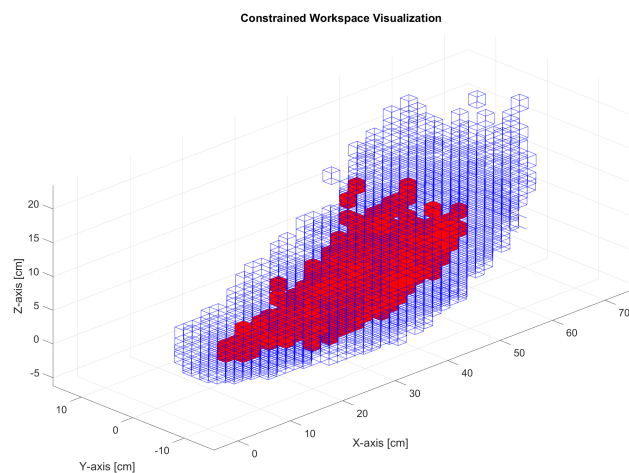


Figure 4.4: The difference between the idealized and accurate model's workspace in the constrained workspace $n_f = 3$. In blue, the workspace with joint angle bounds of $[-45^\circ, 45^\circ]$ is shown, and in red, the workspace with the reduced bounds. The axes refer to the constrained frame of reference (Figure 1.4).

Finally, the prototype, shown in Figure 4.1 (c), is manufactured based on the CAD model. Several additional uncertainties with respect to the model are present due to the play in the joints, the exact lengths of the threaded rods and printed parts, the weight distribution, and deviations in the servo positions. The motor calibration was done using a protractor. Some of the resulting positional errors between the model (Figure 4.1 (b)) and the physical prototype (c) could be quantified with motion-capturing tools, but this exceeds the scope of this work.

4.2 Mechatronic and Mechanic Design

This chapter focuses on the mechatronics and mechanics used in the design. The robot is designed so it fits all mechatronic components, is able to withstand the forces generated by the motors and the robot's weight, and keeps elastic deformation of the parts low.

Compared to the ideal model (Figure 4.1 (a)), the robot is scaled up to a size of 36x60cm, to avoid additional collision modes besides the ones shown in Figure 4.3, especially with the motors (Table 4.1). Due to their simple positional control via a Puls-Width-Modulation (PWM) signal, servos are used for actuating the quadruped (Figure 4.1 (c)). All motors and the motor controller are fitted inside the base, as shown in Figure 4.5 (right). The previous prototype (GAISSER 2024) used six BLS-H50B servo motors from Bluebird (BLUE BIRD TECHNOLOGIES 2024), a motor controller from Spark (SPARKFUN ELECTRONICS 2024), and a BeagleBone (BEAGLEBOARD.ORG 2024) as the microcontroller. All of them were repurposed from the previous prototype. The power supply cables and the USB cable are routed from outside the model. Since the concept is a prototype to show locomotion feasibility, no battery is included. The cables might influence the stability of the robot, though. Therefore, care must be taken to avoid introducing significant forces into the system.

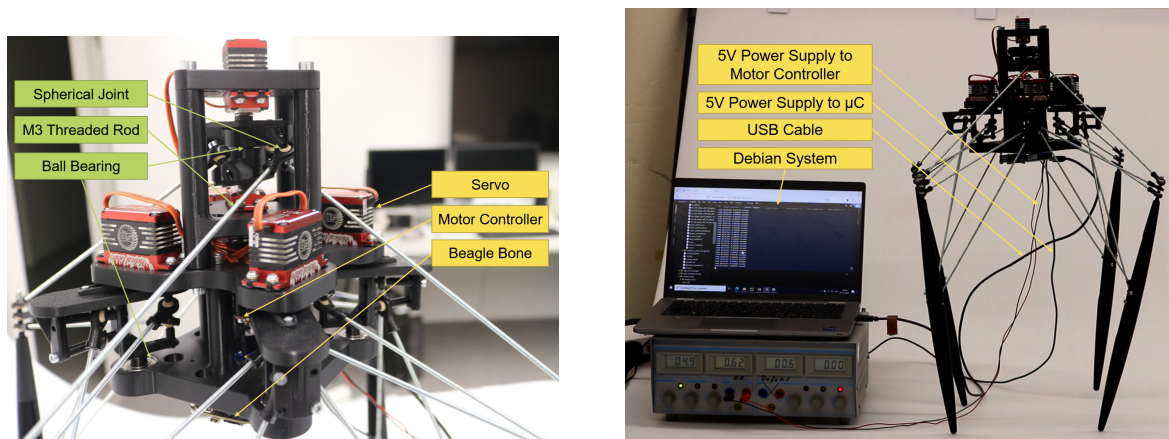


Figure 4.5: Some important components are shown, including important mechanical components (green), and electrical components (yellow).

The servos are controlled via the motor controller's PWM signal. The controller provides only 5V, whereas the servos can operate at up to 8.4V. More torque would, therefore, be attainable with an upgrade to the controller. During operation, the motors draw around 6.2A from the power supply (Figure 4.5). The joint angles are commanded via an I2C bus from the microcontroller, which has a separate 1.2A power supply from the socket. New joint angle commands are sent to the motor controller with a frequency of 50Hz. The servo's input PWM signal is updated with 12-bit resolution at up to 1.6kHz. The limiting factor of how precise the motor positions can be commanded is the servos themselves. Their control

architecture converts the PWM signal to motor movements, which has a dead zone of 0.5° . This means a new joint angle command, which differs from the current joint position by less than 0.5° , is not commanded to avoid oscillations. Without the dead zone, very small changes are commanded, increasing wear, and the slack in the gear system would lead to instabilities of the position control. Unfortunately, this leads to jitter when trying to command slow movements. In practice, a compromise must be found between fast motion with less jitter, further violating the quasi-static assumption, and slow motion with more jitter, which still has some dynamic effects due to abrupt accelerations. A gait cycle of around 20 seconds was found to be a good trade-off.

The robot's structure needs to hold up against the forces generated by these mechatronic components. Besides the screws bearings, and links, all components are 3D printed due to the ease of manufacturing. M3 threaded rods are used for the leg links, which are screwed into the spherical joint's sockets on both ends. It is, therefore, assumed that only normal forces act on the connecting rod. Using Euler's buckling force estimation, the longest rods with a total length of 290.7mm can withstand compressing forces of around 39N as shown in equation 4.1. This exceeds the forces produced by the weight of the robot. If the full weight of the robot acts on one leg, the top link has to endure a maximum of 15N. The motors can produce more force at the top link (66N), but this can only be applied when the robot gets stuck or moves very fast.

$$F_k = \frac{\pi^2 \cdot EI}{L^2} = 39N, \text{ with } I = \frac{\pi \cdot d_k^4}{64}, E = 210GPa \text{ and } d_k = 2,387mm \quad (4.1)$$

The lower motor links have additional bearings, which reduce the load on the internal servo bearings and the elastic deformation, as shown in Figure 4.3 (a). Also, in between the two upper motor links a bearing is placed for similar reasons and to reduce the off-plane error of the motor links. The leg is curved outwards in the middle to house the joints and to withstand lateral forces.

Chapter 5

Validation

After finding gait parameters and modeling the robot, tests are performed both in simulation and on hardware to validate the results. In simulation, the joint angles for each time step are commanded to the actuators. Then, the accuracy of the trajectory is tested by measuring the foot distance space. On hardware, the stability and reliability in real-world conditions are tested qualitatively. Besides the straight crawling, empirically found spinning gaits are also tested.

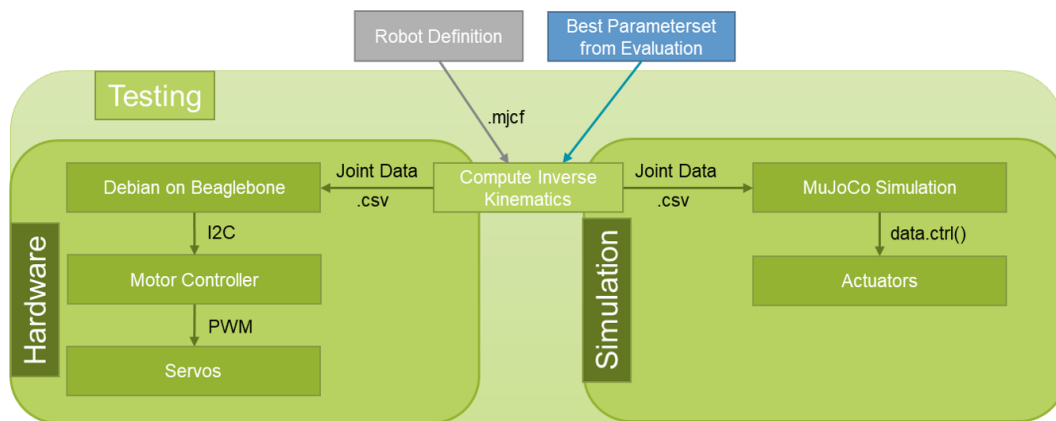


Figure 5.1: Flowchart of the validation procedure. After computing the IK using the robot's definition and the gait parameters from the evaluation, the time series of the joint data for one gait cycle is sent to the microcontroller as well as the MuJoCo simulation, where the robot's crawling capabilities are validated.

5.1 Validation in Simulation

In this chapter, different gaits are tested in simulation. First, two straight crawling gaits are tested, which were found through sampling in Section 3. Then, spinning gaits are tested. The corresponding parameters were found through trial and error, using insight from the sampling.

To simulate walking, the motion capture points used for path generation are replaced by a contact constraint, which models the interaction with the floor. In addition to the impedance parameters "solimp" and "solref", the friction can be set (Table 5.1). Since the foot is modeled spherical and only has a small contact surface, the only significant friction components are in tangential directions. Rolling and torsional friction are neglected. The foot is made of PLA,

and the floor was simulated to be plastic, too, which has a static contact friction of around 0.3. all other parameters are left the same compared to the gait generation.

The simulation uses actuators with a control stiffness value of $k_p = 5000$ and an actuator force range of $[-4\text{Nm}, 4\text{Nm}]$. This is the force range that the servos can provide at 5V (Table 4.1).

Environment	Tunable Parameters in MuJoCo
Floor contact	solref = [0.002, 1] solimp = [0.99, 0.999, 0.001, 0.1, 2] friction = [0.3, 0.3]
Control System	$k_p = 5000$ actuatorfrange = [-4,4]
Time	time step = 0.0001s gait cycle = 20s

Table 5.1: Tunable parameters for floor contact, control system, and time in the Mujoco simulation.

The best results were achieved with a timestep of 0.0001s. With larger timesteps, the simulation tends to be unstable. Also, with shorter gait cycle times than 20s, the dynamics are notable. When starting the simulation, a transient phase occurs. This is the time it takes the solver to converge from the symmetric joint configuration defined in MuJoCo's XML file to the starting configuration of the gait cycle.

5.1.1 Simulation of Crawling Gait

Parameter	Best transition point SM Parameter Set 1	Highest average SM Parameter Set 2
	Value	
a_x	0.06m	0.06m
a_y	0m	0m
g	[1,3,4,2]	[1,3,4,2]
x_2	-0.095m	-0.065m
y_2	0.065m	0.11m
x_3	-0.095m	-0.11m
y_3	-0.065m	-0.08m
x_4	0.17m	0.11m
y_4	-0.05m	-0.095m

Table 5.2: Parameters for two feasible gait determined from sampling the parameter space. On the left is the one with the highest transition point stability margin, and on the right is the one with the highest found average stability margin.

Two crawling gaits are simulated with the parameters in Table 5.2. On the left, the parameters with the best transition point stability margin are shown (Section 3.5.1), and on the right, the configuration, which has the highest found average stability margin of 0.34m (Section 3.5.2). The absolute position of the feet's paths in the ground frame is shown in Figure 5.2. It can be seen that the footpaths are deprived for parameter set 1. Set 2 follows the desired path more accurately.

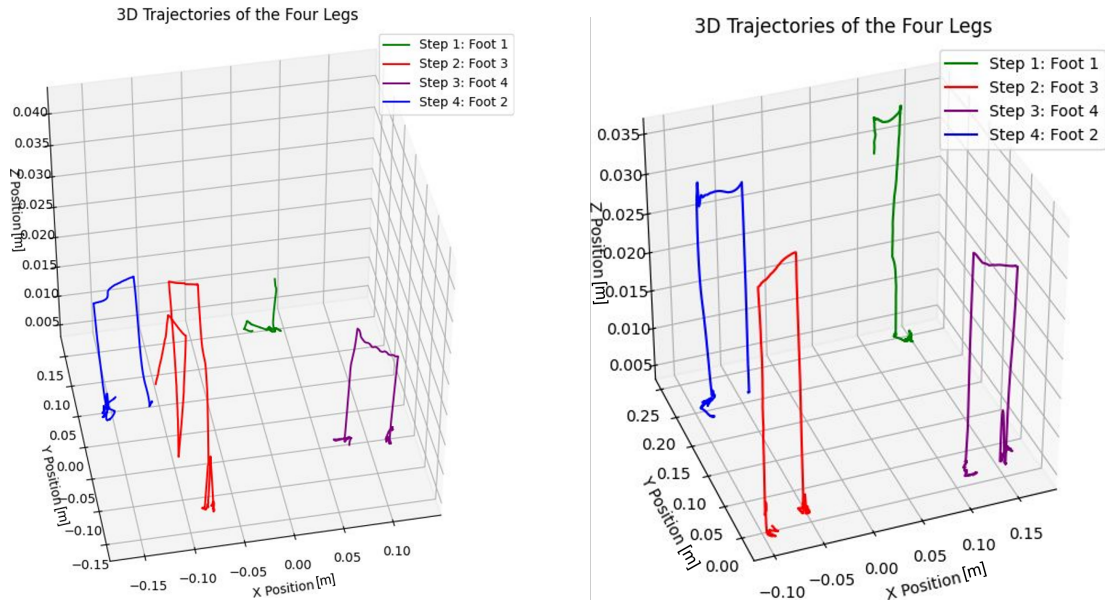


Figure 5.2: The paths of the feet are shown. The absolute positions of the feet are measured in the foot frame. For the gait parameters with the highest margin found in section 3.4.2, the trajectories are deprived (left). With a different set of feasible parameters, with a high average stability margin (right), the IK is accurate enough to allow for stable walking in simulation.

When investigating the relative positions of the feet compared to the desired positions (Figure 5.3), it can be seen that parameter set 1 has a higher foot space error in the range of 0.05m compared to parameter set 2 with an error less than 0.02m. Also, the dynamic settling time can be seen. Figure 5.4 shows the transient phase for parameter set 1 in the foot space (left) and the joint space (right) compared to the desired positions. Strong dynamic oscillations until around 1.3ms. After that, the simulation takes up to a few seconds to fully settle. The paths in Figure 5.2 are shown after the respective settling time has passed to avoid cluttered images, which is why step 1 is partially cut off.

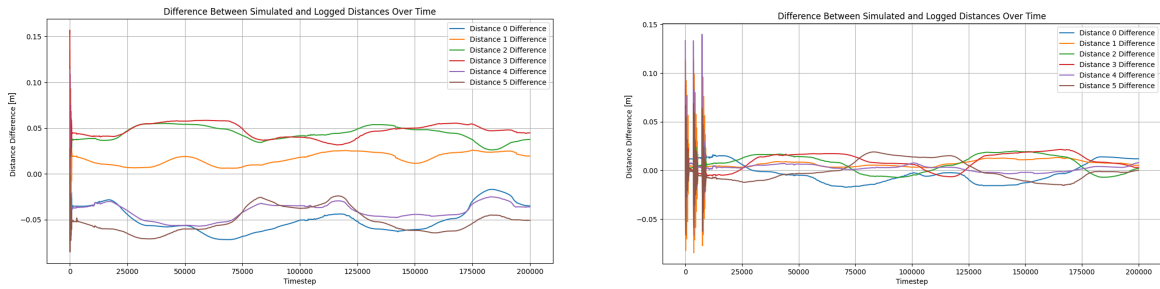


Figure 5.3: The distances of the foot space in simulation compared to the desired distances. On the left are the errors of parameter set 1, and on the right of set 2.

In conclusion, parameter set 1 (Table 5.2 (left)) has large errors in the foot space (Figure 5.3) and can not reproduce the desired crawling gait path (Figure 5.2). The parameters of set 2 (Table 5.2 (right)) allow for stable crawling in simulation and are used for validating the feasibility of crawling on the hardware (Section 5.2).

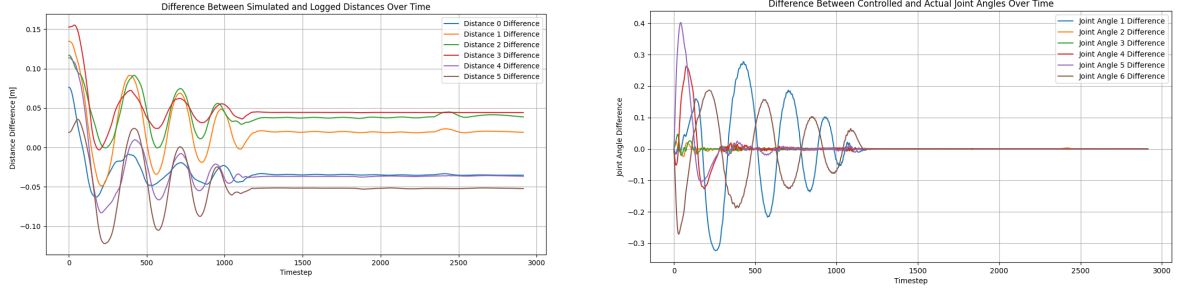


Figure 5.4: The first 3000 timesteps are shown for the errors in the foot distance space (left) and the differences in [rad] between control input and actual joint position (right), both using parameter set 1 to define the desired trajectory. The solver takes around 0.13s to converge, during which dynamic forces are introduced into the system.

5.1.2 Simulation of Spinning Gait

Through trial and error, a reliable parameter set for spinning anti-clockwise was found to be type [1,2,3,4]. With rotation angle $\beta = \pi/8$ and stepping height $h = 0.03\text{m}$ no violating the joint limits occurred for the initial condition shown in Figure 5.5, where the first two legs lag half of the rotation angle β behind.

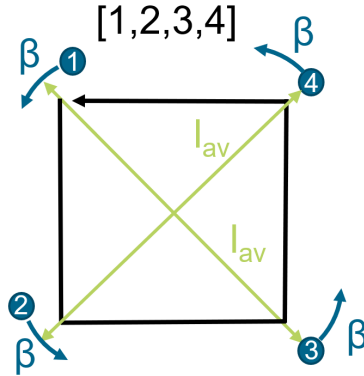


Figure 5.5: Initial configuration of a stable spinning gait. The first two foot positions are behind by half of the rotation angle β .

To calculate the path of the spinning gait, the trajectory calculated in equation (3.4) is transformed to movement along corresponding circles starting at the initial configuration. During each step, the foot f_s is rotated around the origin of the floor frame by angle $\beta = \pi/8$ during each step:

$$p_{s,spinning}(t) = \begin{bmatrix} \cos \theta(t) & -\sin \theta(t) & 0 \\ \sin \theta(t) & \cos \theta(t) & 0 \\ 0 & 0 & 1 \end{bmatrix} p_s(t) \quad (5.1)$$

where

$$\theta(t) = p_s([x, y, z = 0], t) \frac{\beta}{\|a\|} + \phi(f) \quad (5.2)$$

The initial configuration is defined by the phase $\phi(f)$. It is set to $\phi = [0, \pi/2, (\pi + \beta)/2, \pi/2]$. The error in the foot distance space for a full gait cycle without the transient phase is shown in Figure 5.6. This error leads to a sliding motion of the foot opposite of the stepping foot, as shown in Figure 5.7 (left). This leads to a reduced turning angle of around 5° compared to the desired value of $\beta = 22.5^\circ$ during the cycle.

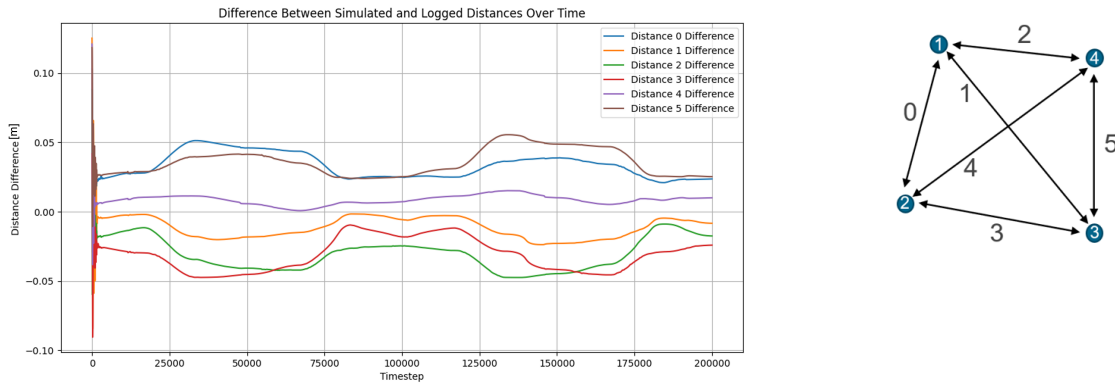


Figure 5.6: The relative foot error during one gait cycle in the spinning gait. The distances are labeled as shown on the right.

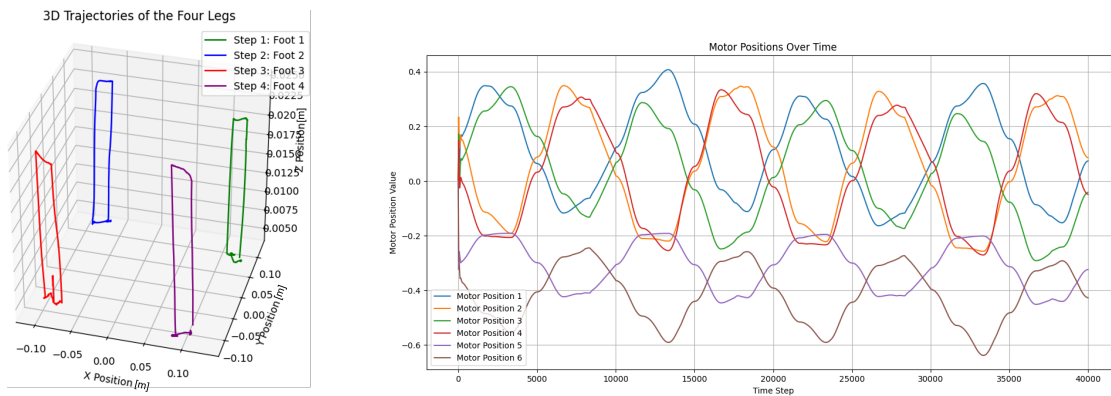


Figure 5.7: Shown on the left are the paths of the feet during spinning in simulation. The absolute positions of the feet are measured in the foot frame in [m]. On the right, the change in motor angles during two gait cycles is shown.

The joint positions at the end of the cycle do not exactly match the joint position at the start. Shown in Figure 5.7 are two gait cycles during which the joint angles are not exactly periodic. In the simulation, the commands repeat after each cycle. The resulting sudden change in desired joint angles, which occurs in between cycles, leads to a dynamic rotation, during which the feet slide on the ground. The next gait cycle starts with the robot rotated by around 10° .

5.2 Validation on Hardware

In this section the gaits are validated on the real robot. The setup used in the experiments is shown in section 4 in Figure 4.5. The time series of the joint data is sent to the beagle bone via a USB cable (Figure 5.1). Both straight crawling and spinning are validated, providing evidence that omnidirectional crawling is feasible.

5.2.1 Validation of Crawling Gait

Using parameter set 2 (Table 5.2 (right)), the crawling gait was first performed on an even ground. The robot is filmed from the top, where the repositioning of the base can be seen. In Appendix A 13 poses during one full gait cycle are shown. The four transition points are shown, as well as the two configurations of each foot, when it is lifted and before it is lowered again. The last picture shows the same configuration as the first one gait cycle later. Also, a test on a curved plastic surface is shown in Appendix A for the same 13 instances during crawling. The uneven ground challenges the model assumption and the robot was only able to walk in specific orientations. Crawling slightly downwards was still feasible while crawling upwards resulted in the back feet not lifting off the ground. The lift-off of foot 1 before and after one gait cycle is shown in Figure 5.8 filmed from the side. The ruler, placed in front of feet 3 and 4, shows that the robot moves forward by around 5cm, a similar amount compared to the simulation (Section 5.1.1) and slightly less than the desired step size of 6cm.

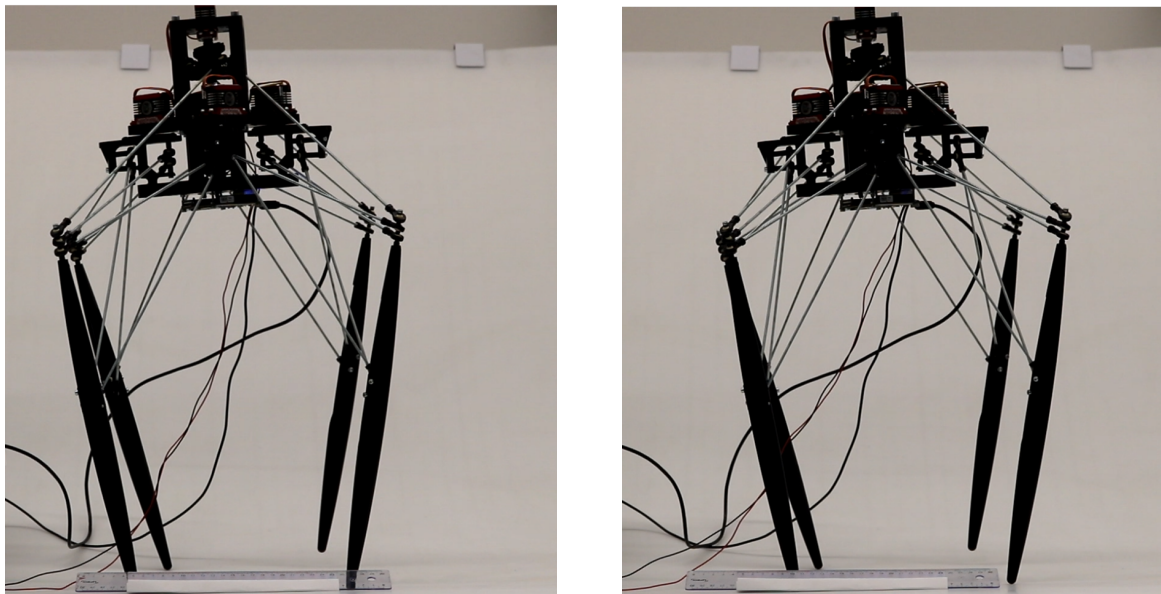


Figure 5.8: Lift off of foot 1 before and after one gait cycle.

5.2.2 Validation of Spinning Gait

The spinning gait was tested on the hardware using the same parameters as in the simulation (Section 5.2.2). It also shows a sliding of the opposing foot, noticed before in the simulation. The fast joint angle change between gait cycles made the robot dynamically rotate around

its central axis, similar to the behavior in the simulation. The orientation of the robot before and after one full gait cycle, including the dynamic rotation in between cycles, is shown in Figure 5.9. Additional poses during spinning are shown in Appendix A. The robot spins by around 10° per gait cycle, meaning one full rotation would take around twelve minutes to complete.

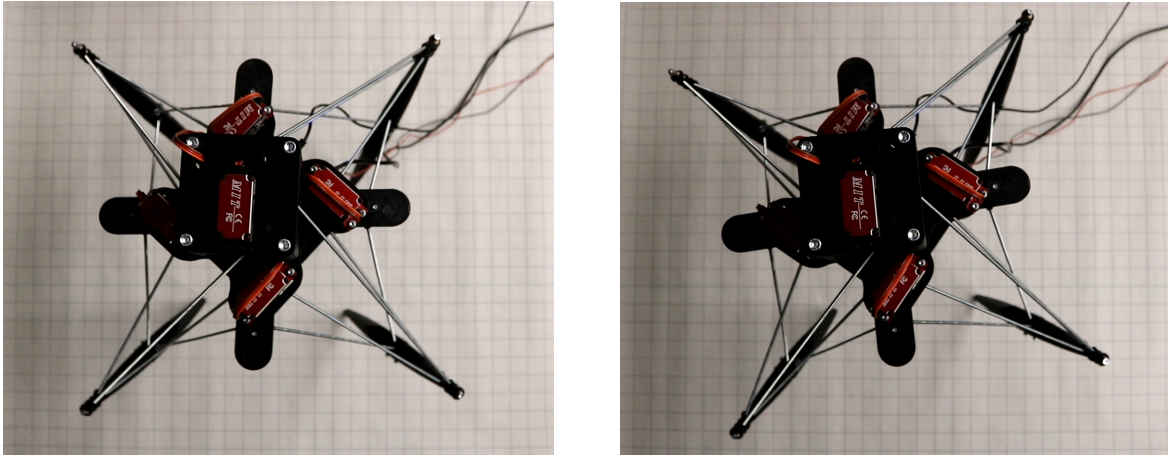


Figure 5.9: Spinning angle before and after one gait cycle including the dynamic rotation between cycles.

Chapter 6

Discussion, Conclusion and Outlook

In his chapter, the results are interpreted and discussed (Section 6.1). Finally, the work is summarized (Section 6.2), and an outlook is given (Section 6.3), explaining which direction might be interesting for future research.

6.1 Discussion

The sampling results (Section 3.5.1) revealed a stability island across configurations mainly in the [1,3,4,2] gait type. Within this gait type, a crab angle of zero degrees ($a_y = 0$) has the most amount of feasible configuration. One reason might be that the foot workspace is larger for straight stepping directions in the foot frame, as shown in Figure 3.2, increasing the number of reachable solutions. When the step vector comes closer to gait type [1,4,2,3] or [1,3,2,4] for larger absolute values of a_y , it results in more unstable gaits for any configuration. As found by MCGHEE 1968, the stability margin for gait type [1,3,4,2] is the highest, which might be a reason why there are far less stable configurations in any other gait type.

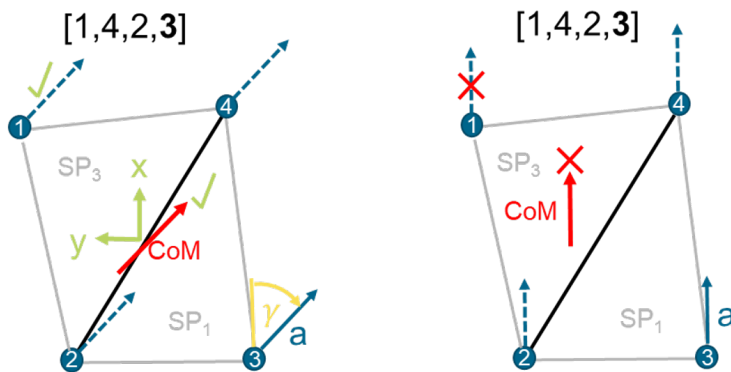


Figure 6.1: The only types of feasible gait parameters for gait type [1,4,2,3] can be seen on the left. The step vector needs to be rotated towards gait type [1,3,4,2] to allow a feasible step with foot 3 so that foot 1 can move next. Shown on the right is a representative parameter set with type [1,4,2,3] which is not feasible, assuming the CoM moves in a similar direction as the stepping foot.

When looking at the conditions (Section 3.1) that need to be fulfilled at the transition points, the scarcity of solutions in all other gait types can be explained. Moving a foot forward usually also moves the CoM forwards, which seems intuitively correct and was observed in

the results (Section 3.5.2). Consequently, moving a foot backward should typically shift the CoM backward. Gait type [1,2,4,3], has both crossing steps set up in such a way, that moving foot 2 and foot 3 forward has to correspond to a backwards movement of the CoM, to be able to lift foot 4 and 1 respectively. Type [1,4,2,3] has one of these forward crossing steps between feet 3 and 1. The way to address this issue is to rotate the step vector by angle γ towards gait type [1,2,4,3] so that this critical step 3 leads to a CoM repositioning from SP3 to SP1 (Figure 6.1). The equivalent reasoning holds for type [1,3,2,4] when stepping with foot 2, which explains the observed feasibility regions for these types.

For the non-crossing gaits [1,2,3,4] and [1,4,3,2], no stable configuration is found for any crab angle and step size. Again a similar reasoning can be applied. Stepping in some arbitrary direction with foot 1 in type [1,2,3,4] requires the CoM to reposition from SP 1 to SP 2. Then, later, a step with foot 3 in the same direction is required assuming the periodic gait cycle. Here the CoM must move from SP 3 to SP 4, which requires the opposite behavior of what was required for step 1. This same reasoning applies to types [1,4,3,2], which makes them unfeasible for straight crawling with a zero-dimensional body space. As shown in section 5.2.2, for spinning gaits these types are adequate. With clockwise spinning type [1,4,3,2] allows the CoM to move in the same direction as the step vector for all four steps. For anti-clockwise spinning [1,2,3,4] was chosen for the same reason.

The most stable gait type $g = [1, 3, 4, 2]$, is also preferred by mammals while walking (MUYBRIDGE 1902), likely to maximize the stability margin and efficiency. The best found initial configuration has a trapezoidal shape, where the front feet have a wider stance than the back feet. On the contrary, many animals, like cats or rabbits, have a wider stance at the back feet. In nature, this might allow them to better jump and run (MUYBRIDGE 1902). For the robot, the configuration instead allows the CoM to start in SP 1 from where it can start the stepping sequence.

Primarily configurations were investigated, where the feet are close to each other. This was mainly done so that most configurations are reachable within the joint limits. It has another benefit. Counterintuitively, a smaller stance inside the defined search space (Section 3.2) usually leads to a higher stability margin for the same stepping height. The main limiting factor for the stability margin is the diagonal edges. With a smaller stance, the robot rotates further along the diagonal edge, which shifts the CoM further inside the support polygon, leading to more stable stepping phases. Also increasing the stepping height usually increases the average stability margin. By turning one of the upper motors the robot leans towards the correct support polygon while the foot is lifted. This helps in finding stable stepping paths.

The stability margin at the transition points is at most 1.14cm for any investigated parameter set and, during the stepping sequence, 3.44cm for the average stability margin, which is quite low. This might be due to the fact, that the geometry optimization (GAISSER 2024) was only performed with respect to the size of the foot workspace and not the combined workspace, which includes the variability of the CoM.

An asymmetry is present both in the number of feasible solutions and the number of reachable solutions towards negative y-components a_y of the step vector. This is likely related to the gait type. The gait type [1,3,4,2] moves feet 1 and 3 first. To touch down inside their workspace, the feet should lift off further back relative to the position of feet 2 and 4. After feet 1 and 3 have stepped, feet 2 and 4 will be further back. This makes the trapezoidal shape look slightly rotated (Figure 3.17 (right)). Since the grid does not account for this rotational asymmetry, a negative y-component of the step vector might correct for this rotation and more reachable and stable configurations lie on the sampling grid.

As shown in the simulation tests (Section 5.1), the error between the desired path and the foot trajectory obtained from the simulation is very notable. The main cause was found to be errors arising from the inverse kinematics (Section 3.4), caused in particular by the high impedance of the "weld" constraints.

The used configuration of parameter set 1 (Table 5.2) deviates by around 0.05m from the desired path, enough to become unstable, while parameter set 2 deviates only by around 0.02m. The reason might be that the latter is closer to the home configuration. Since the "weld" constraints reference the orientation of the feet when all motor angles are zero, deviating further from these orientations induces stronger moments and larger errors in the locomotion path. When studying the errors in Figure 5.3, this pull towards the home configurations can be noticed.

An imbalance is present regarding the strict convergence criterion of 1mm for the dynamic settling (Section 3.3.1), and the trajectory errors in the centimeter range in validation (Section 5.1). By reducing both the impedance of the "weld" constraints and the strictness of the convergence criterion during evaluation, the trajectory error in validating might be reduced without increasing the calculation time of the evaluation.

The fact that parameter set 2 performed better during validation compared to set 1 might be rather due to its closeness to the home configuration and not due to its higher average stability margin. In fact, the average stability margin used for evaluating the full gait cycle path might not be the ideal metric. Configurations with a higher stability margin at the transition points tip over earlier, resulting in a worse average stability margin. This occurs because the margin gets negative at the tipping regions. Setting it to zero during the tipping regions might be a better approach since the quasi-static assumption is violated anyway during the tipping phases.

The discussed reduction of the influence of the "weld" constraints might also reduce the slipping on the floor, which is especially notable when spinning (Section 5.2.2). On the other hand, it might increase the problem of not reaching the exact same joint configuration after one full gait cycle. Its cause when spinning is presumably the singularity, which resembles a twisting of the base. The "weld" constraints should counteract the effects caused by the singularity.

6.2 Conclusion

This research demonstrated the feasibility of stable quasi-static crawling gaits in a quadruped robot with six actuated and no additional passive DoF, like present in most other reduced-DoF designs (Section 1.1). By addressing the challenges posed by the zero-dimensional body space and the high coupling between actuators, this work contributes to the broader field of cost-effective and efficient robotic designs. The approach combined parameterized gait evaluation and experimental validation to establish locomotion patterns for a robot with constrained motion capabilities.

Key outcomes include the identification of feasible gait parameters and stability conditions, achieved through a systematic sampling and evaluation framework. By focusing on transition points during gait cycles, computational complexity was reduced, enabling efficient assessment of potential motion trajectories. The developed prototype successfully implemented and tested these gaits, validating their real-world applicability despite the reduced flexibility compared to traditional quadrupeds.

This study underscores the potential of reduced-DoF quadrupeds in scenarios requiring simplicity, efficiency, and affordability. The insights gained can be extended to dynamic gaits, adaptive control mechanisms, and terrain-adaptive locomotion. Moreover, the methods developed here for gait assessment and robot design provide a foundation for exploring further innovations toward dynamic gaits in these under-actuated robotic systems.

6.3 Outlook

The exploration of feasible gait dynamics in a quadruped robot with six actuated DoF opens several promising directions for future research and development. Expanding upon the methods and discoveries of this work, the following directions present opportunities for advancing the capabilities of reduced-DoF robotic systems:

Expanding Capabilities of Feasibility Map

Incorporating elevation as a variable into the search space can be addressed by storing CoM's x- and y-components instead of stability margins (SM), when pre-evaluating the configurations. The stability margin could be evaluated during sampling, including the information on the elevation. The same 2D transition point sampling approach can also support spinning and turning gaits, and even free gaits, by adapting the step vector and gait type more dynamically. Such capabilities could maybe enable real-time computation of feasible steps, despite the complicated coupled kinematics. Obstacle avoidance, elevation changes, and gait transition capabilities might be attainable.

Enhanced Sampling in 3D Space

A logical extension of the current work involves expanding the sampling methodology to encompass the entire 3D space. This could involve sampling a 9D space using three 3×3 grids or the 6D foot space. Between grid points interpolation techniques can find the evaluation of configurations not on the grid. By storing a 3D feasibility map, also uneven terrain and full stepping trajectories can be evaluated without needing to calculate the inverse kinematics in real time.

Feasibility Maps for Dynamic Gaits

Different feasibility maps can be designed to account for varying combined workspace dimensions. For example, in gaits that include phases with only two feet in contact with the ground ($n_f = 2$), feasible configurations should be assessed regarding dynamic stability definitions. In this combined workspace, five active DoF are available to control the two stepping legs and the location of the CoM. The remaining motor can be used to control the ground reaction forces. Dynamic gaits such as trotting and pacing, where the combined workspace never collapses to a single point, could provide greater flexibility in motion.

Dynamic Walking and Feedback Integration

To enable dynamic walking, an inertial measurement unit (IMU) could be added for real-time feedback. With the presented design, it might also be possible to "see" all four feet from the bottom of the floating base at all times. This could allow for a low-cost solution to measure foot contacts using a single camera or lidar sensor attached to the base. While for crawling, the control system can focus on controlling the foot space and view the body space as a constraint, a more balanced system needs to be implemented for walking, which loosens the exact requirements on the path and takes some active control capabilities to the body space.

Changing the Geometry and Type of the Structure

Finally, design changes could be investigated to enhance the motion capabilities of the robot. Reintroducing asymmetries into the design, which were removed in the previous workspace optimization (GAISSER 2024), might avoid the singular configurations, and could result in a more reliable inverse kinematics calculation. Another promising adaptation is inverting the position of the leg links at the motor links on one side of the leg assembly. This would increase the workspace in the y-direction of the constrained frame and might allow larger steps. Also, optimizing the geometry to increase the combined workspace of the base and the feet, and ultimately the ability to efficiently move in various gaits, might be a promising direction for future research.

This work sets a robust foundation for realizing these advancements, potentially enabling more capable, efficient, and adaptive robotic systems in the future.

Appendix A

Image Sequences for Crawling and Spinning Gaits

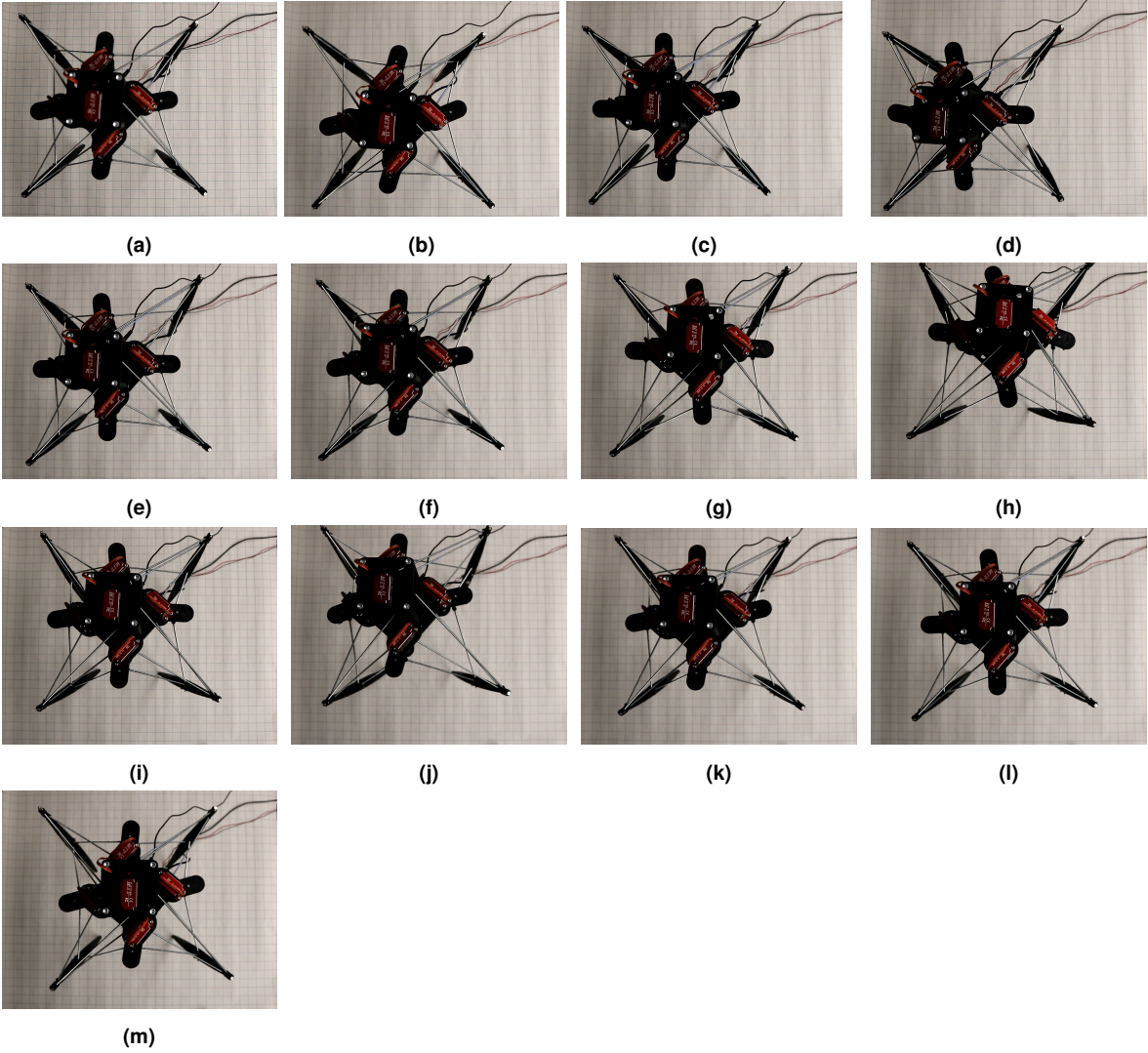


Figure A.1: Full gait cycle of a feasible crawling gait from the top with three pictures for each step. Figure (m) is in the same configurations as Figure (a) one cycle later.

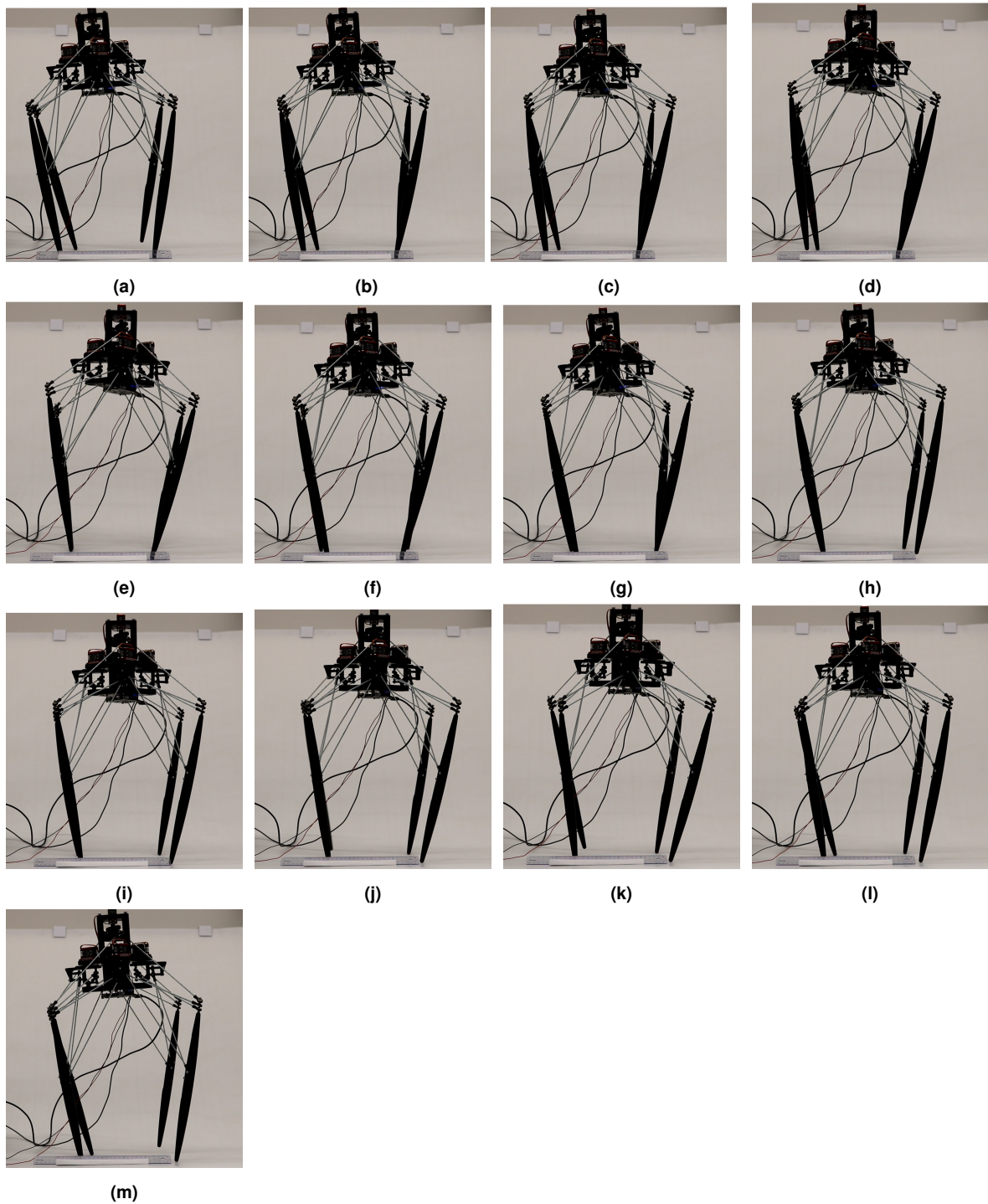


Figure A.2: Full gait cycle of a feasible crawling gait from the side with three pictures for each step. Figure (m) is in the same configurations as Figure (a) one cycle later.

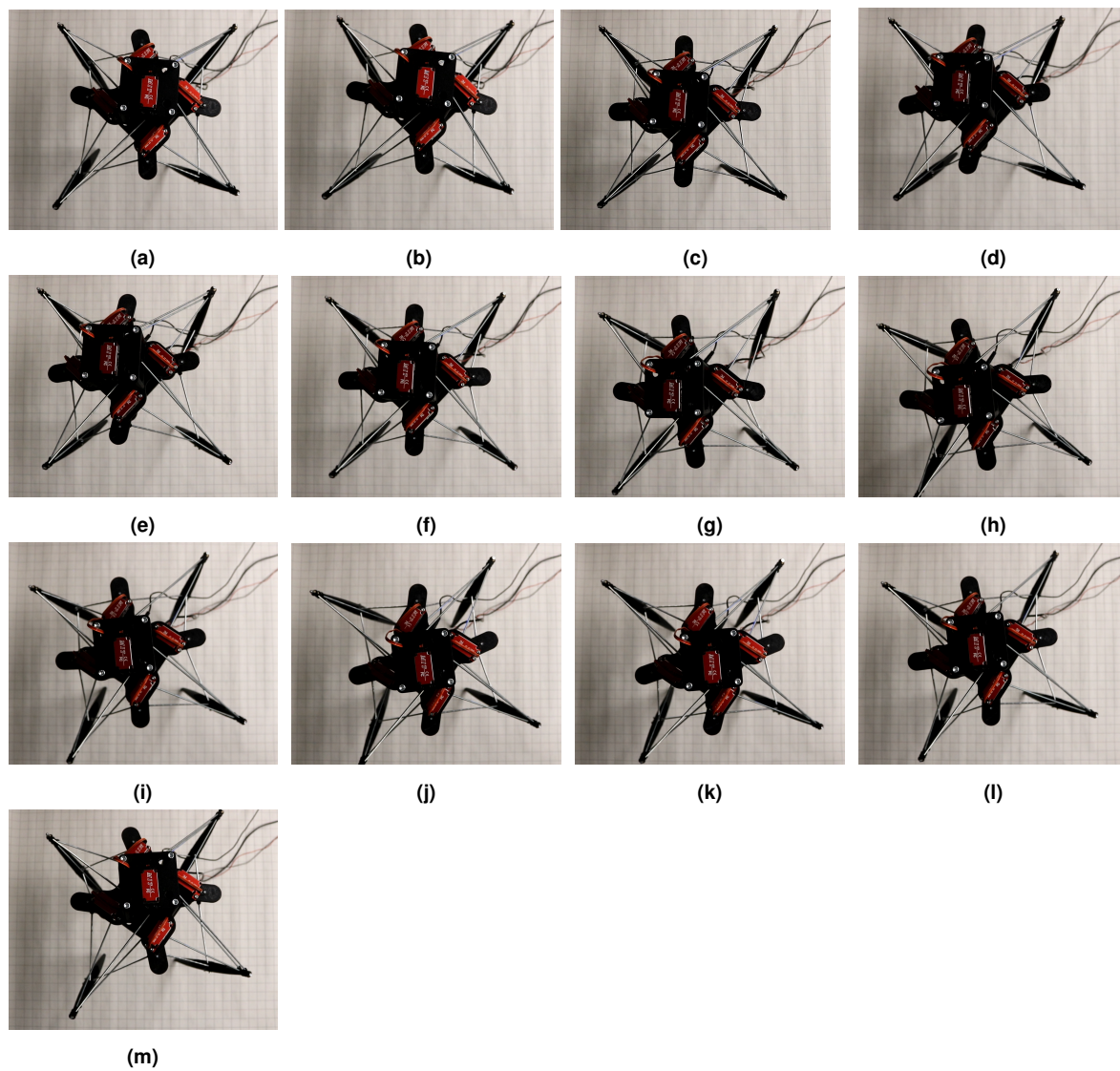
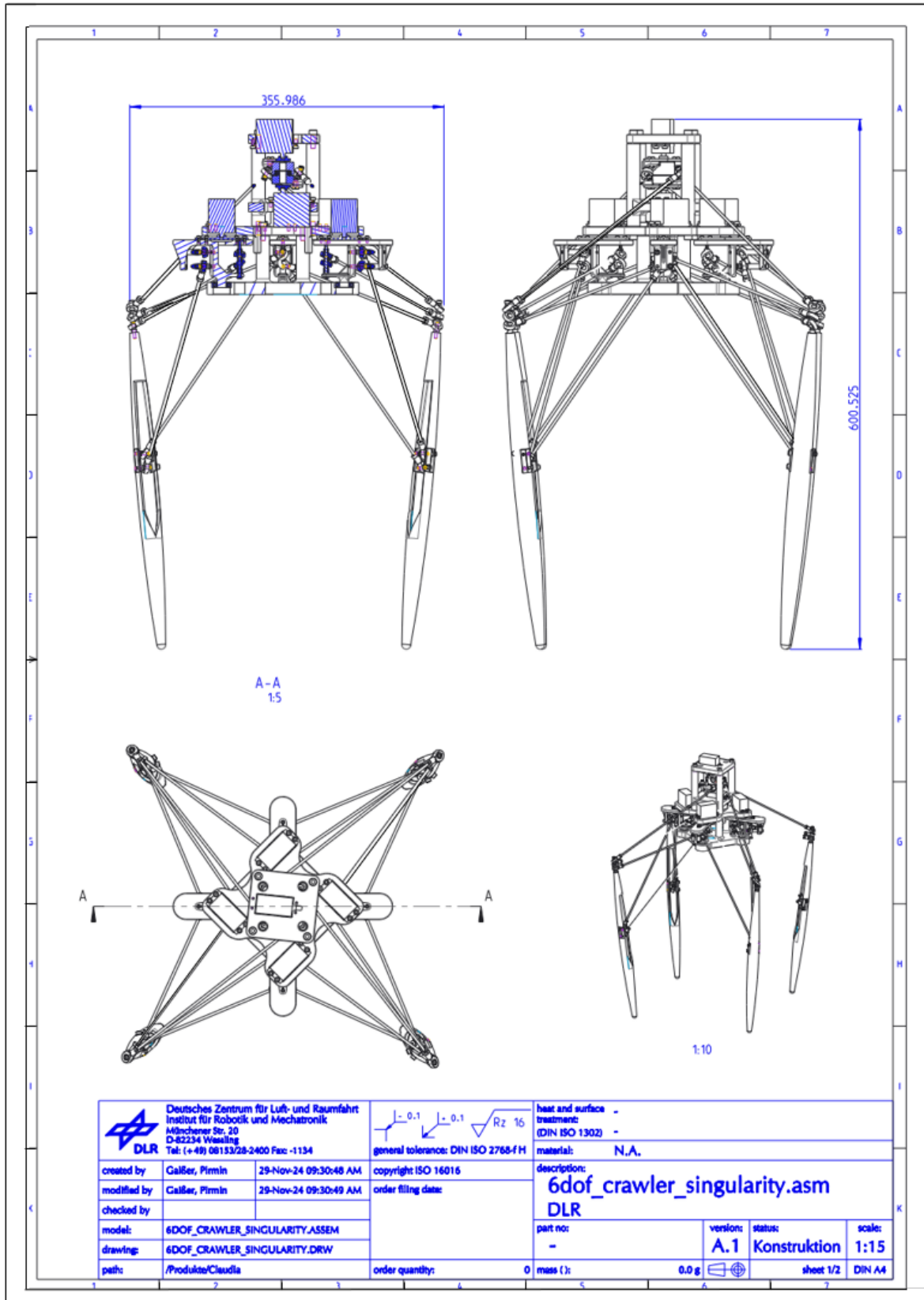


Figure A.3: Full gait cycle of a feasible turning gait from the top with three pictures for each step. Figure (m) is in the same configurations as Figure (a) one cycle later.

Appendix B

Technical Drawing



(a)

Figure B.1: Technical Drawing of the Robot

Benennung:		- Struktur-Stückliste ohne Schrauben und ECAD				
BG-Zei.-Nr.:		A - ARTIKEL_NR:1 - A05				
Pos.	Gegenstand in Ebene	part number	Typ	Stück	Material	Common_name
1	1 TOPLINK_ASM	0001396322	ASSEMBLY	4	N.A.	
	1 GEWINDESTANGEM3_271	0001406601	PART	1	EN AW-2007	gewindestangem3_271.prt
	2 2024_07_29_14_17_18_0823	0001406602	PART	2	EN AW-2007	2024_07_29_14_17_18_0823.prt
2	1 MOTORLINK_UPPERASM_INST	0001396328	ASSEMBLY	1	N.A.	
	1 MOTORADAPTER_BLUEBIRD	0001408825	PART	1	ABS	motoradapter_bluebird.prt
	2 KUGELLAGERADAPTER	0001408415	PART	4	PLA_3Dprinted	kuellageradapter.prt
	3 AUSSEN	0001411008	PART	1	PLA_3Dprinted	motorlink_top_modified.prt_INST
	4 2024_07_29_14_17_18_0839	0001406597	PART	2	EN AW-2007	2024_07_29_14_17_18_0839.prt
3	1 MOTORLINK_UPPERASM	0001396328	ASSEMBLY	1	N.A.	
	1 MOTORLINK_TOP_MODIFIED	0001411008	PART	1	PLA_3Dprinted	motorlink_top_modified.prt_INST
	2 MOTORADAPTER_BLUEBIRD	0001408825	PART	1	ABS	motoradapter_bluebird.prt
	3 LG_RK_618_10x19x5		PART	1	steel	lg_rk_618_10x19x5.prt
	4 KUGELLAGERADAPTER	0001408415	PART	4	PLA_3Dprinted	kuellageradapter.prt
	5 2024_07_29_14_17_18_0839	0001406597	PART	2	EN AW-2007	2024_07_29_14_17_18_0839.prt
4	1 MOTORLINK_LOWERASM	0001396327	ASSEMBLY	4	N.A.	
	1 MU_SK_DIN439_M03		PART	3	St	mu_sk_din439_m03.prt
	2 MOTORADAPTER_BLUEBIRD	0001408825	PART	1	ABS	motoradapter_bluebird.prt
	3 MOTORLINK_MODIFIED	0001397570	PART	1	PLA_3Dprinted	motorlink_modified.prt
	4 KUGELLAGERADAPTER	0001408415	PART	8	PLA_3Dprinted	kuellageradapter.prt
	5 KT_DISTANZHUELSE_03-06		PART	3	Nylon	KT_DISTANZHUELSE_03-06
	6 2024_07_29_14_17_18_0839	0001406597	PART	4	EN AW-2007	2024_07_29_14_17_18_0839.prt
5	1 LEGLINK_UPPERASM	0001396331	ASSEMBLY	8	N.A.	
	1 GEWINDESTANGEM3_203	0001406606	PART	1	EN AW-2007	gewindestangem3_203.prt
	2 2024_07_29_14_17_18_0823	0001406602	PART	2	EN AW-2007	2024_07_29_14_17_18_0823.prt
6	1 LEGLINK_LOWERASM	0001396330	ASSEMBLY	8	N.A.	
	1 GEWINDESTANGEM3	0001406604	PART	1	1.4301 / X5CrNi18-10	gewindestangem3.prt
	2 2024_07_29_14_17_18_0823	0001406602	PART	2	EN AW-2007	2024_07_29_14_17_18_0823.prt
7	1 LEG_ASM	0001396324	ASSEMBLY	4	N.A.	
	1 MU_SK_DIN439_M03		PART	2	St	mu_sk_din439_m03.prt
	2 LEG_MODIFIED	0001397568	PART	1	PLA_3Dprinted	leg_modified.prt
	3 KUGELLAGERADAPTER	0001408415	PART	10	PLA_3Dprinted	kuellageradapter.prt
	4 KT_DISTANZHUELSE_03-06		PART	3	Nylon	KT_DISTANZHUELSE_03-06
	5 2024_07_29_14_17_18_0839	0001406597	PART	5	EN AW-2007	2024_07_29_14_17_18_0839.prt
8	1 BASEASM	0001396325	ASSEMBLY	1	N.A.	
	1 SERVO_HITBOX	0001396582	PART	6	Steel	servo_hitbox.prt
	2 LG_RK_619_10x22x6		PART	4	steel	lg_rk_619_10x22x6
	3 BASE_UPPER	0001396320	PART	1	PLA_3Dprinted	base_upper.prt
	4 BASE_TOP	0001408928	PART	1	PLA_3Dprinted	base_top.prt
	5 BASE_SLANTED_	0001395300	PART	1	PLA_3Dprinted	base_slanted_.prt
	6 BASE_LOWER	0001408503	PART	1	PLA_3Dprinted	base_lower.prt

 Deutsches Zentrum für Luft- und Raumfahrt Institut für Robotik und Mechatronik Münchener Str. 20 D-82234 Weßling Tel: (+49) 08153/28-2400 Fax: -1134		general tolerance: DIN ISO 2768-fH copyright ISO 16016 order filing date:	heat and surface treatment: (DIN ISO 1302) - material: N.A. description: 6dof_crawler_singularity.asm DLR
created by: Gaißer, Pirmin modified by: Gaißer, Pirmin checked by: model: 6DOF_CRAWLER_SINGULARITY.ASSEM drawing: 6DOF_CRAWLER_SINGULARITY.DRW path: /Produkte/Claudia	29-Nov-24 09:30:48 AM 29-Nov-24 09:30:49 AM	order quantity: 0	part no: - version: A.1 status: Konstruktion scale: 1:15 mass (): 0.0 g sheet 2/2 DIN A4

(a)

Figure B.2: Part List of the Robot

List of Figures

1.1	All six gait sequences as defined by MCGHEE 1968 relative to the crawling direction marked with the green arrow (left) and the visualization of the gait diagram for crawling sequence [1,3,4,2] (right). Each leg is lifted individually, and four transition points occur.	2
1.2	(a) Body space (b) Foot space (c) Combined space with $n_f = 3$ (d) Combined space with $n_f = 2$	3
1.3	The structure of the robot (left). One of the four leg assemblies is marked in blue. The structure of a leg assembly (right). The joints are drawn as circles, crosses, and squares, and the links as lines. The scale is non-dimensionalized and shows the relative proportions (GAISSER 2024).	6
1.4	Shown are the coordinate systems used in this work. The body frame is shown in blue, the green one is fixed at the ground, and the orange frame is used to describe the constrained foot space. The dotted lines mark the distances between the stance feet.	6
2.1	The main structure of the work. After defining the motion space, the feasibility of different gaits is assessed, paths for them are generated, translated to motor commands via inverse kinematics, and then tested on the simulation and hardware.	7
2.2	Relationship between active joint angle space and foot space. The feasibility assessment is simpler when creating the trajectories in the parameterized foot space.	8
2.3	Parameterized gait assuming one gait cycle. Each step can be described by the step vector a , the gait type and the path p	9
2.4	Shown on the left is the distance space with four variables (blue dotted lines) and grid space with six variables (black dots). On the right is a visualization showing that small angle changes γ relative to the stepping direction are included in the 6D-grid space.	10
3.1	Definition of the feet indices and corresponding SP. The long diagonals are dotted and mark the intersection of opposing SP.	14

3.2	Shown on the left is the 3D representation of the constrained workspace estimation using the idealized model from (GAISSER 2024). The dimensions relate to the constrained frame on reference in [cm]. The red faces are in the xy-plane, corresponding to transition point configurations. On the right is the overlap between the sampling grid (green squares) and the workspace (red) visualized. Adjacent stance feet are average width l_{av} apart from each other. .	16
3.3	The front left foot is always foot defined as 1. The step vector always has a positive x-component, which is larger than the y-component. For angles γ outside the range of $[-45,45]$, the crossing gaits change type and the coordinate system is rotated to fit the notation.	17
3.4	Visualization of separation of the gait assessment into three parts. The separation reduces the feasible solutions step by step so that more computationally intense evaluations only need to be done for good candidates.	17
3.5	Flow chart of the configuration evaluation.	18
3.6	Information stored in precomputation for each configuration.	19
3.7	Show is the path the simulation takes when sampling the configurations. The snake-like path is followed back and forth until all configurations are evaluated.	19
3.8	The Feasibility map of foot 3 (left) and foot 4 (right). When all other feet are in the center location of their grids. The x-axis points towards the right. Shown are the evaluations when moving the respective foot around in the grid.	20
3.9	Flow chart of the sampling evaluation.	21
3.10	After the first foot takes a step of size a , the configuration is shifted back onto point P_1	21
3.11	Flow chart of the path evaluation.	22
3.12	Top view of five different type 1 singular configurations with the same distances in the foot space (blue lines), for lower motor angles of 30° (a), 15° (b), 0° (c), -15° (d), and -30° (e)	23
3.13	The four different assembly modes of a single leg assembly, where (a) is the used configuration (GAISSER 2024)	24
3.14	Shown are two error modes where the solver converges to the wrong assembly mode. The one on the left is prevented by using "weld" constraints at the feet, and the right by introducing limit constraint at the active joint angles.	24
3.15	Shown the number of initial configurations that have feasible transition point configurations for the crossing gait-type $g=[1,3,4,2]$ different step vectors. By allowing the vector a to point in all directions, all four crossing gait types are covered. The borders, where the gait type changes, are marked by green dotted lines. The green square shows where the most feasible solutions lie in.	26
3.16	Figure (a) shows the number of searchable solutions, (b) the number of reachable solutions, (c) the number of stable solutions, and (d) the number of reachable solutions from a different angle to show the asymmetry. The assessments are done by sampling all four transition points of all configurations for the most promising gait parameter set, which is the green region in Figure 3.15 (right).	27

3.17	Shown on the left is the best transition point stability margin in [m] across all configurations for a specific parameter set on the grid. The transition point stability margin describes the lowest stability margin across all four transition points. Shown on the right are the four initial configurations, whose transition point stability margins are the highest with a step size of 0.06m in the x-direction.	28
3.18	Shown are the feasibility maps on the sampling grid. The step vectors on each map indicate that for the given configuration (3.9), both the stability and reachability constraints are fulfilled at all four transition points.	29
3.19	Shown is gait type (orange) and the stability margin (blue) during the full cycle for the initial configuration defined in equation (3.9). The green area is where the robot is statically stable and red lines mark the tipping regions. . .	30
3.20	Shown is the position of the CoM in [m] and the joint angles in [rad] for three gait cycles. The x-component of the CoM moves forward by three step sizes. . .	30
4.1	The three main stages along the mechanical design. (a) is the idealized model, used in previous work for optimization, and (b) is the Creo model, from which the physical prototype is built (c).	33
4.2	The range of motion α of the used spherical joint KBRM-03 from IGUS 1964, shown on the left is 30° , and two of them must be placed at least 8mm apart from each other. The resulting error distribution between the idealized and accurate model's foot position is shown on the right.	35
4.3	Collision configurations of lower motor link and leg links (a), neighboring top links (b), and upper motor link and top link (c).	35
4.4	The difference between the idealized and accurate model's workspace in the constrained workspace $n_f = 3$. In blue, the workspace with joint angle bounds of $[-45^\circ, 45^\circ]$ is shown, and in red, the workspace with the reduced bounds. The axes refer to the constrained frame of reference (Figure 1.4).	35
4.5	Some important components are shown, including important mechanical components (green), and electrical components (yellow).	36
5.1	Flowchart of the validation procedure. After computing the IK using the robot's definition and the gait parameters from the evaluation, the time series of the joint data for one gait cycle is sent to the microcontroller as well as the MuJoCo simulation, where the robot's crawling capabilities are validated.	39
5.2	The paths of the feet are shown. The absolute positions of the feet are measured in the foot frame. For the gait parameters with the highest margin found in section 3.4.2, the trajectories are deprived (left). With a different set of feasible parameters, with a high average stability margin (right), the IK is accurate enough to allow for stable walking in simulation.	41
5.3	The distances of the foot space in simulation compared to the desired distances. On the left are the errors of parameter set 1, and on the right of set 2.	41

5.4	The first 3000 timesteps are shown for the errors in the foot distance space (left) and the differences in [rad] between control input and actual joint position (right), both using parameter set 1 to define the desired trajectory. The solver takes around 0.13s to converge, during which dynamic forces are introduced into the system.	42
5.5	Initial configuration of a stable spinning gait. The first two foot positions are behind by half of the rotation angle β	42
5.6	The relative foot error during one gait cycle in the spinning gait. The distances are labeled as shown on the right.	43
5.7	Shown on the left are the paths of the feet during spinning in simulation. The absolute positions of the feet are measured in the foot frame in [m]. On the right, the change in motor angles during two gait cycles is shown.	43
5.8	Lift off of foot 1 before and after one gait cycle.	44
5.9	Spinning angle before and after one gait cycle including the dynamic rotation between cycles.	45
6.1	The only types of feasible gait parameters for gait type [1,4,2,3] can be seen on the left. The step vector needs to be rotated towards gait type [1,3,4,2] to allow a feasible step with foot 3 so that foot 1 can move next. Shown on the right is a representative parameter set with type [1,4,2,3] which is not feasible, assuming the CoM moves in a similar direction as the stepping foot.	47
A.1	Full gait cycle of a feasible crawling gait from the top with three pictures for each step. Figure (m) is in the same configurations as Figure (a) one cycle later.	53
A.2	Full gait cycle of a feasible crawling gait from the side with three pictures for each step. Figure (m) is in the same configurations as Figure (a) one cycle later.	54
A.3	Full gait cycle of a feasible turning gait from the top with three pictures for each step. Figure (m) is in the same configurations as Figure (a) one cycle later.	55
B.1	Technical Drawing of the Robot	58
B.2	Part List of the Robot	59

List of Tables

1.1	Selection of quadrupeds with different numbers of actuated and passive DoF and their availability for controlling foot and body workspace dimensions . . .	4
2.1	Advantages and disadvantages of parameterizing the active joint angle space and the foot space.	8
2.2	Advantages and disadvantages of assessment methods.	9
2.3	Advantages and disadvantages of sampling methods.	11
2.4	Advantages and disadvantages of Paths.	11
2.5	Advantages and disadvantages of CLIK vs QP-optimization solver.	12
2.6	Advantages and disadvantages of simulation and hardware testing.	12
3.1	The constraints concerning stable crawling, including the stability at transition points and stepping phases the constraints concerning the foot space, including the conditions on the velocities of stance feet, and the height of the stepping foot.	13
3.2	The requirements for the specific design choices and assumptions used in this work, including the average stability margin during the full gaits cycle, staying inside the workspace limits set by the joint angles and the conditions on the height of the stepping foot.	14
3.3	The boundaries of parameters including the step vector a , gait type g , initial position and path height h used for the parameter search and parameters used for path discretization in time and space.	15
3.4	Hardware specifications including the processor, its speed, the memory, and the used version of Python and MuJoCo.	20
3.5	Tunable parameters for constraints of the Mujoco simulation (DEEPMIND 2024)	23
4.1	Some important Hardware specifications including the part count, weight, key dimensions and cost estimation.	34
5.1	Tunable parameters for floor contact, control system, and time in the Mujoco simulation.	40
5.2	Parameters for two feasible gait determined from sampling the parameter space. On the left is the one with the highest transition point stability margin, and on the right is the one with the highest found average stability margin.	40

Bibliography

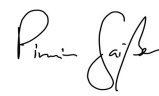
- BEAGLEBOARD.ORG, (2024). *BeagleBone Black - A low-cost, community-supported development platform*. <https://beagleboard.org/black>. Accessed: 2024-11-18.
- BLUE BIRD TECHNOLOGIES, (2024). *BLS-H51B Helical Gear High Speed Brushless Servo*. https://www.blue-bird-model.com/products/17_54.htm. Accessed: 2024-11-18.
- BONEY, R., SAINIO, J., KAIVOLA, M., SOLIN, A., and KANNALA, J., (2022). *RealAnt: An Open-Source Low-Cost Quadruped for Education and Research in Real-World Reinforcement Learning*. eprint: 2011.03085. URL: <https://arxiv.org/abs/2011.03085>.
- BUEHLER, M., BATTAGLIA, R., COCOSCO, A., HAWKER, G., SARKIS, J., and YAMAZAKI, K., (1998). “SCOUT: a simple quadruped that walks, climbs, and runs”. In: *Proceedings. 1998 IEEE International Conference on Robotics and Automation*. IEEE, pp. 1707–1712. ISBN: 0-7803-4300-X. DOI: 10.1109/ROBOT.1998.677408.
- CARPENTIER, J., MIRABEL, J., and TEAM, (2024). *Pinocchio: Fast Forward and Inverse Dynamics for Robotics and Animation*. <https://stack-of-tasks.github.io/pinocchio>. Accessed: 2024-11-24.
- DEEPMIND, (2024). *MuJoCo: Multi-Joint dynamics with Contact*. Version 3.2.2. URL: <https://mujoco.org/>.
- GAISSER, P., (2024). *Workspace Analysis of a Highly Coupled Quadruped Robot with Six Actuated Degrees of Freedom*.
- GONZALEZ DE SANTOS, P., GARCÍA, E., and ESTREMER, J., (2006). *Quadrupedal locomotion: An introduction to the control of four-legged robots*. London: Springer. ISBN: 184628306X.
- HAMLIN, G. J. and SANDERSON, A. C., (1994). “A novel concentric multilink spherical joint with parallel robotics applications”. In: *The institute of electrical and electronics engineers 1994 – 1994 IEEE International Conference*, pp. 1267–1272. DOI: 10.1109/ROBOT.1994.351313.
- IGUS, (1964). *Blase, Magreth; Blase, Günther*. Mülheim, Köln, Germany. URL: https://www.igus.de/product/igubal_KBRM_KBLM?artnr=KBRM-03.
- KANEKO, M., ABE, M., and TACHI, S., (1986). “Basic considerations of the degrees of freedom of multi-legged locomotion machines”. In: *Advanced Robotics 1.2*, pp. 101–116. ISSN: 0169-1864. DOI: 10.1163/156855386X00021.
- KANNER, O. Y., ODHNER, L. U., and DOLLAR, A. M., (2014). “The design of exactly constrained walking robots”. In: *2014 IEEE International Conference on Robotics and Automation (ICRA)*. IEEE, pp. 2983–2989. ISBN: 978-1-4799-3685-4. DOI: 10.1109/ICRA.2014.6907289.
- KATZ, B., DI CARLO, J., and KIM, S., (2019). *2019 International Conference on Robotics and Automation (ICRA)*. Piscataway, NJ: IEEE. ISBN: 9781538660270.
- KING, B., (2022). “Kinematic Design and Optimization of a Quadruped Robot with Six Actuated DoF”. Master Thesis. Dortmund: Technische Universität.
- MAHAPATRA, A., ROY, S. S., and PRATI HAR, D. K., (2020). *Multi-body Dynamic Modeling of Multi-legged Robots*. Singapore: Springer Singapore. ISBN: 978-981-15-2952-8. DOI: 10.1007/978-981-15-2953-5.

- MCGHEE R. B.; Frank, A. A., (1968). "Optimum Quadruped Creeping Gaits". PhD thesis. Los Angeles: University of California.
- MERLET, J., (2006). *Parallel robots*. 2nd ed. Vol. 74. Solid mechanics and its applications. Dordrecht and Boston MA: Kluwer Academic Publishers. ISBN: 1402041322.
- MUYBRIDGE, E., (1902). *Animals in Motion*. London: Chapman & Hall.
- NASA, (2022). "Multi-Link Spherical Joint". 11635107.
- OROCOS, (2024). *PyKDL: Python Bindings for the Kinematics and Dynamics Library*. <https://www.orocos.org/kdl>. Accessed: 2024-11-24.
- PTC, (2022). *Creo Parametric*. Version 7.0. PTC Inc. 121 Seaport Blvd, Boston, MA 02210, USA. URL: <https://www.ptc.com/en/products/cad/creo>.
- RAIBERT, M. H., (1986). *Legged robots that balance*. The MIT Press series in artificial intelligence. Cambridge Mass.: MIT Press. ISBN: 0262181177.
- SEIDEL, D., HERMANN, M., GUMPERT, T., LOEFFL, F. C., and ALBU-SCHÄFFER, A., (2020). *2020 IEEE Aerospace Conference: Yellowstone Conference Center, Big Sky, Montana, March 7-14, 2020*. Piscataway, NJ: IEEE. ISBN: 9781728127347. DOI: 10.1109/AERO47225.2020. URL: <https://ieeexplore.ieee.org/servlet/opac?punumber=9161765>.
- SONG, M. J., DING, C. J., and YU, C. J., (2015). "Workspace Analyzing for Hybrid Serial-Parallel Mechanism of a New Bionic Quadruped Robot". In: *Applied Mechanics and Materials* 713-715, pp. 837–840. DOI: 10.4028/www.scientific.net/AMM.713-715.837.
- SPARKFUN ELECTRONICS, (2024). *SparkFun Qwiic Motor Driver - Dual H-Bridge (DRV8833)*. <https://www.sparkfun.com/products/15316>. Accessed: 2024-11-18.
- YONEDA, K., OTA, Y., ITO, F., and HIROSE, S., (2000). "Construction of a quadruped with reduced degrees of freedom". In: *26th Annual Conference of the IEEE Industrial Electronics Society*. IEEE, pp. 28–33. ISBN: 0-7803-6456-2. DOI: 10.1109/IECON.2000.973121.
- YONEDA, K., (2007). "Light Weight Quadruped with Nine Actuators". In: *Journal of Robotics and Mechatronics* 19.2, pp. 160–165. ISSN: 0915-3942. DOI: 10.20965/jrm.2007.p0160.
- ZHANG, X., LANG, L., WANG, J., and MA, H., (2015). "The quadruped robot locomotion based on force control". In: *The 27th Chinese Control and Decision Conference (2015 CCDC)*. IEEE, pp. 5440–5445. ISBN: 978-1-4799-7017-9. DOI: 10.1109/CCDC.2015.7161766.

Disclaimer

I hereby declare that this thesis is entirely the result of my own work except where otherwise indicated. I have only used the resources given in the list of references.

Garching, December 2, 2024

A handwritten signature in black ink, appearing to read "Pini Goff". The signature is written in a cursive style with a large initial 'P' and 'G'.

(Signature)